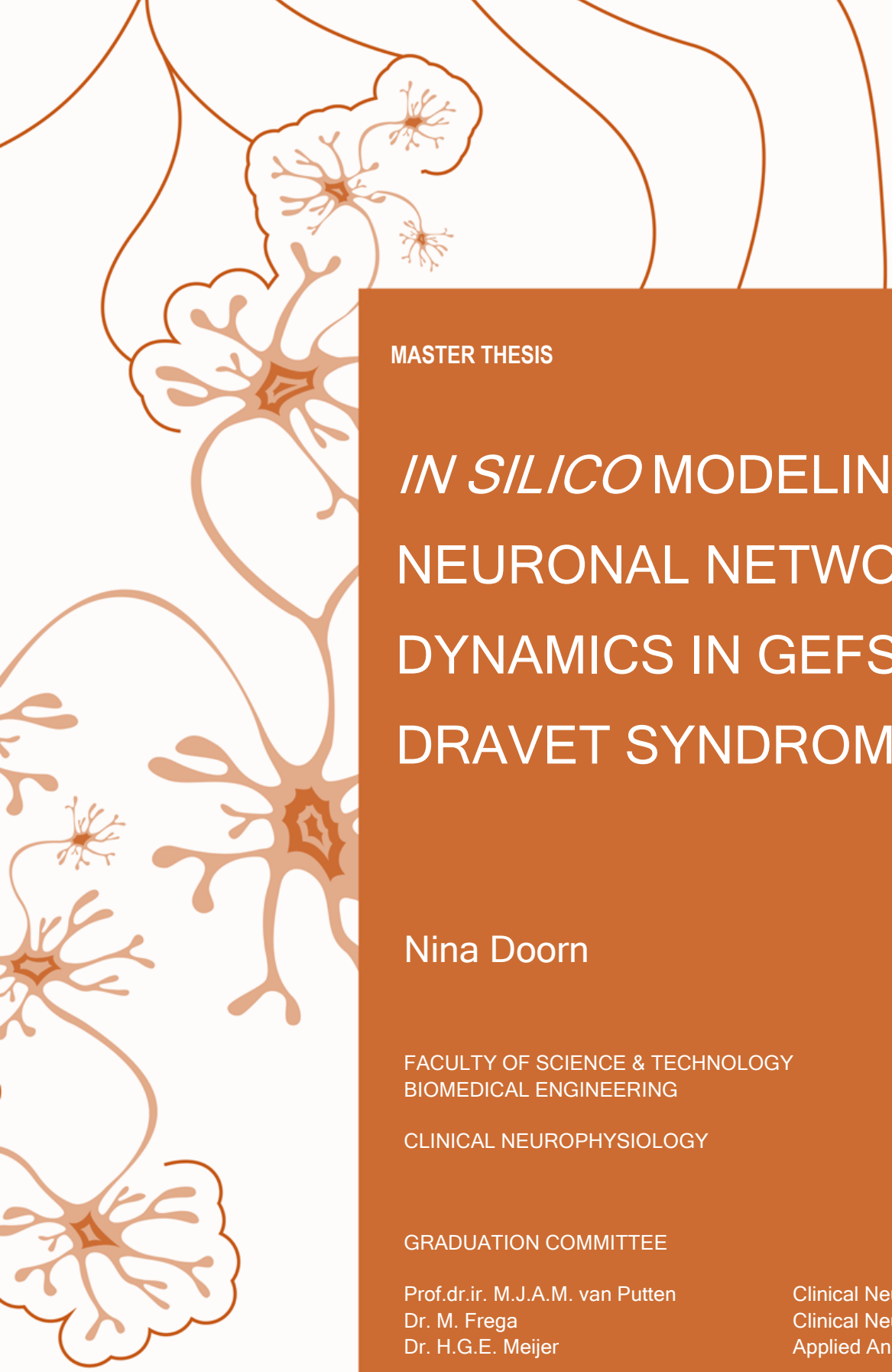

MASTER THESIS

IN SILICO MODELING OF NEURONAL NETWORK DYNAMICS IN GEFS+ AND DRAVET SYNDROME

Nina Doorn

FACULTY OF SCIENCE & TECHNOLOGY
BIOMEDICAL ENGINEERING

CLINICAL NEUROPHYSIOLOGY

GRADUATION COMMITTEE

Prof.dr.ir. M.J.A.M. van Putten	Clinical Neurophysiology / MST
Dr. M. Frega	Clinical Neurophysiology / Radboud
Dr. H.G.E. Meijer	Applied Analysis

01-07-2021

UNIVERSITY OF TWENTE.

Acknowledgments

The process of my master's assignment was truly an extension of my education. I have learned many new things, discovered new interests, and developed new skills, for all of which I am very grateful. Moreover, I have greatly enjoyed doing my master thesis and working with my supervisors and my colleagues in the Clinical Neurophysiology group. Therefore, I would like to acknowledge those who contributed.

First of all, I would like to thank my daily supervisor, Michel van Putten, for his never-ending enthusiasm for my work. Our weekly meetings were always full of enervating discussions leading to many new ideas and insights on both sides. Michel greatly contributed to my newfound passion for computational modeling in neuroscience. He was always eager to see my progress and share that progress with others in the group or the research field. So thank you, Michel, for making my project truly enjoyable. Next, I want to thank my supervisor, Hil Meijer, for repeatedly getting me through periods of being stuck. Hil always took the time to hear my problems and always managed to instantly help me make great strides in my research. Even when I temporarily lost confidence in my project, Hil took the time to show me the essence of computational modeling and give me a final boost. So thank you, Hil, for the many great tips and speeches. I also want to thank my supervisor, Monica Frega. Even though we did not speak much, her clear and passionate explanation about the cultured neurons made me choose this extremely interesting subject for my thesis. In the end, her feedback regarding the cultures considerably helped me to improve my report. So thank you, Monica, for still wanting to be my supervisor, even though time was limited. I also want to thank Eline van Hugte and Nael Nadif Kasri for providing me with so much experimental data, for our discussions and the answers to all my questions, and for the interest in my project.

Moreover, I want to thank the other students of the group, the PhD candidates, and Marloes Levers, for making my time at the group enjoyable and enervating. They were always open for questions and discussions while enjoying a cup of coffee or lunch in the sun. Because I could easily spar with them about problems or ideas, I often quickly obtained new insights for my project. I especially want to thank Eva Voogd for making me feel welcome in the group from the beginning and making every day fun.

Abstract

Rationale Generalized Epilepsy with Febrile Seizures Plus (GEFS+) and Dravet Syndrome (DS) are two epilepsy syndromes in the same spectrum, with divergent clinical phenotypes, that can both be caused by a mutation in the voltage-gated sodium channel of neurons. The pathophysiological mechanisms underlying GEFS+ and DS are far from understood. *In vitro* neuronal networks derived from healthy control- and patient stem cells show distinct differences in spontaneous electrical network activity. The processes underlying these differences are challenging to unravel. Here, we use an *in silico* model to elucidate the role of sodium channel mutations and network dynamics in explaining the *in vitro* observations.

Approach We combine existing models to obtain a model of 100 thermodynamic Hodgkin-Huxley neurons, including spike-frequency adaptation, sparsely connected via plastic AMPA and NMDA synapses. We first calibrate parameters such that the model can replicate the behavior observed from healthy (WT) neuronal networks. For GEFS+ and DS, we modify the voltage-gated sodium channel dynamics.

Results Our model faithfully reproduces the behavior of the WT cultures. We found that changes in sodium channel dynamics were not sufficient to reproduce the behavior of the GEFS+ and DS cultures. Additional downscaling of the synaptic weights and adaptive mechanisms resulted in network behavior similar to that of GEFS+ and DS cultures.

Significance Our results suggest that homeostatic synaptic plasticity, modeled by downscaling of the synaptic weights, has a considerable influence on the behavior of GEFS+ and DS neuronal networks. This could potentially explain the large inter-patient variability in clinical phenotypes and tractability. To further validate these hypotheses, the influence of homeostatic plasticity needs to be evaluated *in vitro* and the computational model needs to be expanded to incorporate long-term plasticities.

List of Abbreviations

AEDs	Anti-Epileptic Drugs
AP	Action Potential
DIV	Days in Vitro
DS	Dravet Syndrome
EPSC	Excitatory Post-Synaptic Current
GEFS+	Generalized Epilepsy with Febrile Seizures Plus
HH	Hodgkin-Huxley
hiPSC	human induced Pluripotent Stem Cells
LIF	Leaky Integrate-and-Fire
MEA	Micro-Electrode Array
MNBD	Mean Network Burst Duration
MNBR	Mean Network Burst Rate
NB	Network Burst
PSIB	Percentage of Spikes in Burst
PSP	Post-Synaptic Potential
SNIC	Saddle Node on an Invariant Circle
STD	Short Term Depression
STF	Short Term Facilitation
WT	Wild Type

Contents

1 | Introduction

Epilepsy is one of the most common neurological disorders in the world, affecting more than 68 million people worldwide [1]. In many patients, epilepsy can be treated with anti-epileptic drugs (AEDs) or brain surgery, but a substantial part of the cases remains intractable. In some patients, the disorder may be truly untreatable. In other patients, finding the right treatment is complicated by our incomplete understanding of the pathophysiological mechanisms underlying some forms of epilepsy. Even for cases that are treatable with AEDs, finding the effective drugs and the optimal dose can take long periods of trial and error [2].

Two such poorly understood epilepsy disorders are Generalized Epilepsy with Febrile Seizures Plus (GEFS+) and Dravet Syndrome (DS). GEFS+ is a familial epilepsy spectrum characterized by generalized tonic-clonic seizures. Usually, there is a predisposition to febrile seizures. Febrile seizures are associated with body temperatures above 38 °C in children younger than 5 years [3]. GEFS+ patients continue to have these seizures past the age of 5 or progress to show afebrile seizures [4]. Dravet syndrome (DS) is a severe form of GEFS+ and is characterized by more frequent and prolonged febrile seizures [4]. Seizures of DS patients are often unresponsive to anti-epileptic therapy and can even be exacerbated by some of the conventional therapies [5]. Moreover, DS can cause mild to severe and permanent intellectual disability, especially if the seizures are not controlled [3]. Both GEFS+ and DS can be caused by a mutation in the SCN1A gene, which is one of the most commonly mutated genes associated with epilepsy [4, 6]. The SCN1A gene encodes for the α-1 subunit (the pore) of the voltage-gated sodium channel. These channels have a crucial role in neuron excitability [7]. Mutations in the SCN1A gene can lead to a large variety of clinical phenotypes [6] and even identical mutations can lead to divergent phenotypes with varying severities [4]. The pathophysiological mechanisms underlying GEFS+ and DS, and their divergent phenotypes, remain largely unknown.

To gain more insight into these mechanisms, human *in vitro* models can be used. The recent developments in human induced pluripotent stem cell (hiPSC) technology with the possibility to differentiate patient stem cells into neurons allow us to make these models of human neuronal diseases [8]. The group of dr N. Nadif Kasri used this method to culture excitatory neuronal networks of healthy control subjects (WT), a patient with GEFS+, and a patient with DS (both with an SCN1A mutation). The behavior of the networks was captured by measuring the spontaneous electrical network activity using micro-electrode arrays (MEAs). There are distinct differences between the activity observed from the WT, GEFS+, and DS cultures, as shown in Figure 1. Similar to the distinct phenotype of GEFS+ and DS in patients, they also appear to have a defined signature in *in vitro* neuronal networks. These features can be used to gain insight into the pathophysiological network behavior. However, because not all processes are easily controlled or measured *in vitro*, it remains difficult to identify the exact mechanisms that produce this pathophysiological network behavior.

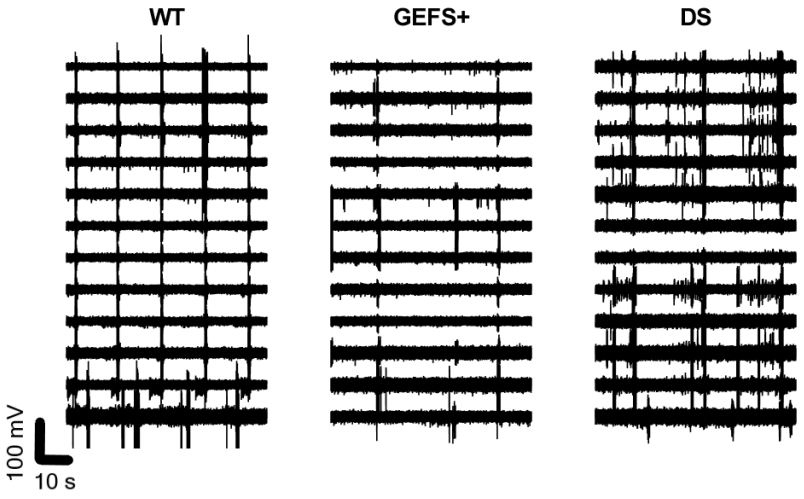

Figure 1: Extracellular voltage recordings from 12 MEA electrodes (stacked signal) of three neuronal cultures. The WT cultures show regular bursts of network activity with almost no activity in the inter-burst period. GEFS+ cultures show bursting at a lower rate with more out-of-burst activity and less similarity between electrodes. DS cultures show bursts with a longer duration and even more out-of-burst activity. Data kindly provided by dr. N. Nadif Kasri.

In silico models can be used to gain insight into the specific mechanisms underlying the behavior seen in *in vitro* models. Such neuronal computational models have been used widely to aid in the fundamental understanding of single neuron dynamics [9–14], and neuronal network behavior [15–25]. Single neuron models of GEFS+ and DS [26–28] neglect network behavior, and their findings cannot explain the undisclosed features of GEFS+ and DS. Neuronal network models of *in vitro* systems do include network dynamics and can simulate realistic network behavior. However, most of these models use simple neuron models, such as the Leaky integrate-and-fire- (LIF), or the Izhikevich neuron model [29]. These simple models suffice when focusing on network dynamics but if network behavior is hypothesised to arise from detailed ion channel dynamics, like in GEFS+ and DS, we need a more detailed neuron model. Therefore, this thesis will aim to use a biophysically realistic neuron in an *in silico* network model of WT, GEFS+, and DS neuronal cultures. The first objective is to develop a model that can simulate the behavior observed in WT cultures, using a neuron model that includes ion-channel dynamics. The second objective is to explore changes to the neuron and network model dynamics that result in a model that can simulate behavior observed from GEFS+ and DS cultures. In this way, we can identify candidate mechanisms for the characteristics we observe *in vitro* and use this knowledge to make a substantiated hypothesis about the mechanisms underlying GEFS+ and DS.

2 | Background

2.1 Genetic epilepsies

Epilepsy is a group of neurological disorders characterized by an endured predisposition of the brain to generate epileptic seizures [30]. An epileptic seizure is a transient change in behavior, experience, or motor function due to abnormal, excessive, or disproportionately synchronous neuronal activity [30]. Epilepsy can be caused by brain injury, metabolic conditions, or a genetic predisposition to seizures. More than 500 genetic loci are associated with various forms of epilepsy [31]. Epilepsy-associated genes often encode ion channels and synaptic proteins. The mechanisms through which these mutations lead to epilepsy are largely unknown [32]. Childhood epileptic encephalopathies, such as Dravet Syndrome, are increasingly linked to specific mutations. These disorders are also some of the most severe and intractable classes of epilepsy [31]. Many of the identified mutations are in the SCN1A gene, encoding the voltage-gated sodium channel α_1 subunit ($Na_v1.1$). This gene appears to be an epilepsy *superculprit* since more and more phenotypes associated with a mutation in this gene are identified [6]. These phenotypes range from benign to extremely severe. A generally benign condition is Generalized Epilepsy with Febrile Seizures Plus (GEFS+). In GEFS+, febrile seizures continue to occur beyond the age when they typically abate. Moreover, patients may experience afebrile seizures, including generalized tonic-clonic, absence, and atonic seizures [33]. On the severe side of the spectrum is Dravet Syndrome (DS). DS is a rare and intractable epilepsy syndrome associated with cognitive deficit and developmental delay in language, motor function, learning, and social skill [34]. DS usually presents itself around six months of age in a previously normally developing baby. DS generally first shows hemiclonic or generalized febrile status epilepticus. Until the first life year, babies experience recurrent convulsive febrile episodes that may occur as frequently as every 1-2 months. Between the ages of 1 and 4, other seizure types can emerge, such as myoclonic seizures, complex partial, and absence seizures [4]. GEFS+ and DS show clinical similarities, including the frequent occurrence of febrile seizures. Moreover, in some families with heterozygous SCN1A mutation, both disorders are present. This suggests that GEFS+ and DS represent a clinical spectrum of the same disease [35]. More than 330 mutations of the SCN1A gene have been registered to this date [6]. These mutations can cause different types of defects in the voltage-gated sodium channel and may lead to epilepsy in different ways. The different mechanisms may explain why some cases are often treatable, like GEFS+, and some are not, like DS. To describe the wide range of possible dysfunctions of the voltage-gated sodium channel associated with GEFS+ and DS, the most important findings are summarized below.

Generalized Epilepsy with Febrile Seizure Plus (GEFS+)
SCN1A mutations in GEFS+ patients are often inherited. Multiple researchers investigated the effect of several mutations on the sodium channel functioning. Spampanato et al. [36, 37] cloned three mutations into the $Na_v1.1$ rat gene and determined the electrophysiological properties of the resulting channel. One mutation resulted in enhanced slow inactivation of the sodium current, resulting in a persistent-like current. The second mutation showed accelerated recovery from inactivation. These would theoretically both result in hyperexcitability of the neurons, which could lead to epilepsy. A third mutation showed a hyperpolarized shift in the voltage dependence of activation and inactivation of the sodium channels. The shift in activation would result in neuron hyperexcitability, while the shift in inactivation would result in hypoexcitability of the neuron. Other research characterized four mutations associated with GEFS+ using patch-clamp recordings of recombinant human SCN1A heterologous expressed in cultured mammalian cells [33, 38]. One mutation resulted in a depolarizing shift in the voltage dependence of activation, leading to hypoexcitability of the neuron. A second mutation showed accelerated recovery from inactivation, which would lead to hyperexcitability of the neuron. A third showed complete loss of function, which would lead to neuron hypoexcitability. The last mutation showed altered channel inactivation, resulting in a persistent sodium current and thus neuron hyperexcitability. Volkers et al.[39], using mutagenesis in human-derived cells, found that an SCN1A mutation resulted in a hyperpolarizing shift in the voltage dependence of activation, slower recovery from inactivation, and increased persistent sodium current. There are thus mixed biophysical gating effects that, together, might cause GEFS+. This mix of effects can cause either hypo- or hyperexcitability in the neurons. Hyperexcitability of

neurons causes hyperexcitability of the brain and can thus cause seizures. It is not obvious, however, how hypoexcitability of neurons can lead to epilepsy. One hypothesis is that inhibitory neurons are affected more severely and become more hypoexcitable than excitatory neurons. This could alter the excitation/inhibition balance in the brain, leading to general hyperexcitability.

Dravet syndrome (DS)
SCN1A mutations in DS patients often arise *de novo*. Most of the mutations result in haploinsufficiency [40]. The Caterall group [41] showed in a mouse model of the disease that interneurons, but not pyramidal neurons, had dramatically reduced sodium current density. They suggest that the $Na_v1.1$ is the primary functional sodium channel in interneurons and that glutamatergic pyramidal neurons rely on other sodium channels. They hypothesize that DS is due to disturbed excitation/inhibition balance [42]. This hypothesis is challenged by models using hiPSC derived neurons obtained from DS patients [43, 44]. These models show an increased sodium current density and hyperexcitability in both inhibitory and excitatory neurons. Further analysis of the sodium channels revealed delayed inactivation of the channels, leading to a persistent-like sodium current. Some mutations resulted in a significant hyperpolarizing shift in the voltage-dependence of activation compared to WT. These neurons showed higher spontaneous spiking and greater excitability than WT neurons [43]. Interestingly, mutations that resulted in nonfunctional sodium channels also led to higher sodium current density in the neurons. The research showed upregulation of voltage-gated sodium channel mRNAs and thus upregulation of other brain sodium channel transcripts in response to the SCN1A haploinsufficiency. This could also explain the inter-individual variability among patients with heterozygous mutations. Depending on differences in genetic background, this upregulation may differ.

2.2 hiPSC derived neuronal cultures on MEAs

In vitro neuronal models are a promising tool to study the complex behavior of healthy and pathological neuronal networks. Apart from measuring the electrophysiological properties of individual neurons, cultures can also be used to measure the activity of large networks to get insight into neuronal network development and organization [45]. Micro-electrode arrays (MEAs) are cell culture dishes with embedded micro-electrodes. MEAs allow for non-invasive, simultaneous, and long-term recordings of a population of neurons at a millisecond time scale. A MEA can detect changes in the extracellular field caused by the current flows from the closest neurons and other nearby cells. Extracellular action potentials can be measured when electrodes are placed in the vicinity ($\pm$ 100 µm) of the Action Potential (AP), or spike, origin [46]. MEAs can measure the spontaneous activity of neuronal networks. This activity is usually characterized by spontaneous regular network bursting activity. Network bursts (NBs) are defined as synchronized bursts of firing activity in neurons spread throughout the whole network, separated by longer intervals of almost complete silence. The properties of the bursting behavior, like the burst rate and the burst duration, are often characteristic of the neuronal network and can give insight into the dynamics [8]. We therefore often extract features from the MEA recordings, like the NB rate and the percentage of spikes in NBs, to describe the network dynamics. MEAs have been widely used to measure activity from a range of different neuronal culture systems, like primary cell cultures and brain slices, mainly taken from rats [8]. With the advancement in human induced pluripotent stem cell (hiPSC) technology, it also became possible to make *in vitro* models of neuronal networks that more closely resemble the human brain. hiPSCs are cells, usually derived from fibroblasts or leukocytes, that have been 'reprogrammed' back into an embryonic-like pluripotent state. From this pluripotent state, the cells can give rise to an almost unlimited source of any type of human cell [47]. Because these cells have the same genotype as the human subject, they can be used to establish patient-specific *in vitro* models of genetic disorders. These models can be used for diagnosis and treatment optimization for individual patients [48]. Moreover, these models can be used to gain insight into the disease mechanisms [49]. Recently, there have been technical advances enabling the differentiation of pluripotent cells towards relatively pure populations of specific neuronal subtypes such as excitatory and inhibitory neurons [50]. hiPSC derived neurons can form a unique model of neurological diseases with a genetic origin because they capture the patient's entire genetic background, which may influence disease onset and progression [51]. An example of such a model is that by Frega et al. [52], where they used hiPSCs to obtain a model for Kleefstra syndrome. They cultured hiPSC derived neuronal networks on MEAs to elaborately study the network behavior. The properties of spontaneous electrical activity were significantly different between healthy control and patient lines but were consistent across different control lines or different

patient lines [8, 52]. Quraishi et al. [53] used hiPSC derived neuronal networks on MEAs to obtain a model for a childhood epilepsy syndrome. Both studies uncovered a robust and defined phenotype, elucidated several important disease mechanisms, and proposed new treatments. This illustrates the potential of hiPSC derived neuronal networks cultured on MEAs.

2.3 Computational modeling

Computational modeling is a powerful tool to identify candidate mechanisms underlying (pathological) neuronal processes. Using physiologically relevant models, computational modeling enables generating hypotheses, making new predictions, and refining experiments [54]. This section will shortly discuss previous research on computational models of epilepsy and cultured neuronal networks to better understand where this study fits in. Moreover, we consider a biophysical neuron model including ion channel dynamics and other important mechanisms to be modeled.

2.3.1 Computational models of epilepsies and cultured neuronal networks

Several computational models have already been made to study GEFS+ and DS. Spampanato et al. [26] made computer simulations of single neurons, including functional effects of three mutations they found in patients with GEFS+. They used an Hodgkin-Huxley (HH) neuron model, including ion channel dynamics, to model shifts in voltage dependency and accelerated recovery from inactivation of the sodium channel. The model showed that each mutation resulted in an increased tendency to fire repetitive APs. Kahlig et al. [27] used a Markov model of a neuron to model the effect of a particular GEFS+ SCN1A mutant. They found that this resulted in an increased persistent sodium current. Berecki et al. [28] modeled the result of a DS mutation that had severe outcomes in patients. They used whole-cell patch-clamp measurements to get experimental data from mammalian cells cotransfected with the mutant sodium channel. An HH-type neuron model was used to incorporate hyperpolarizing shifts of the activation and inactivation of the sodium channel and enhanced fast inactivation. Simulations showed the model neurons were hyperexcitable by a left shift in their rheobase relative to control.

These studies all used patch-clamp data of single neurons to fit activation, inactivation, and time constants. However, the resulting simulations were not compared to experiments. Moreover, they looked at mammalian cells transfected with mutant sodium channels. This has limitations, as the neurons did not have other characteristics of human patient neurons, including possible protein processing or modulatory activity that changes the function of a given mutation. Also, they only studied single neurons, ignoring the relevance of network dynamics in epilepsy.

Several researchers developed computational models of cultured networks of neurons; they focused on neuron interaction, unaddressed in the studies mentioned above. Gritsun et al. [15–17] simulated the behavior of rodent cultured neuronal networks on MEAs using a random connectivity network model with 5000 Izhikevich neurons. Spontaneous activity was either induced using noise injection or with endogenously active neurons. A simple synapse model of inhibitory and excitatory synapses with short-term facilitation and depression was included. This model reproduced bursting behavior with features in the same ranges as observed experimentally. Masquelier and Deco [21] researched the adaptive mechanisms at play in excitatory cortical neuron cultures using a computational model and *in vitro* rodent neuron assemblies. Experimentally, they observed spontaneous NBs with relatively constant durations and inter-NB-intervals in a binomial distribution. Their computational model consisted of 800 LIF neurons. The neurons were fully connected via a model of AMPA and nonlinear NMDA synapses. The neurons were subjected to spike-frequency adaptation in the form of an afterhyperpolarizing current. Moreover, every neuron received a substantial amount of synaptic noise. The synapses were subjected to short term facilitation and depression (STF and STD). With this model, they were able to recreate the complex statistics of the NBs. By varying the contributions from the different fatigue mechanisms, they found that STD is responsible for quenching the NB, STF for promoting multiple subsequent NBs, and adaptation for forcing a long (experimentally observed) inter-NB-interval. Park et al. [20] also modeled NBs observed in *in vitro* networks of rodent neurons. They investigated the variability of burst dynamics according to a wide range of parameters such as connectivity, recovery time constants, and noise. They modeled 64 (one neuron for each MEA electrode) LIF neurons with injected noisy current. They used a simple linear synapses model that was subjected to STD and STF. The neurons

were locally connected in a probabilistic way determined by the Euclidean distance between them. They found that the burst profile is largely dependent on STD, while connectivity and noise play a smaller role.

These computational models reproduced several of the characteristics observed from *in vitro* neuronal networks. However, these studies used cultures of rodent cells, while hiPSCs might be more suitable to model a human brain since there are significant differences between human and rodent neuron cultures [55]. Moreover, these models and other models of neuronal cultures [19, 22, 25] used simple neuron models that do not include ion channel dynamics. This limits the modeling of diseases caused by changes in ion channel dynamics. To our knowledge, currently, no *in silico* model including a detailed neuron model that can simulate an *in vitro* network of neurons derived from human cells exists.

2.3.2 Biophysical neuron and network models

Cellular neuron models allow us to study how changes at the molecular level, like mutations in ion channels, affect neuronal behavior. The highest level of detail is obtained by compartmental modeling. Compartmental modeling is well suited to obtain detailed information about the cell and accurately simulate extracellular voltage in the proximity of the neuron. However, compartmental modeling is computationally expensive, especially if networks with many neurons need to be simulated. Since we want to simulate large networks of neurons in this research, a slightly simpler neuron model is preferred. A one-compartment physiologically realistic neuron model is the Hodgkin-Huxley model.

The Hodgkin-Huxley model
The traditional Hodgin-Huxley (HH) model [56] describes a single neuron as a modified electrical circuit where the charge carriers are sodium (Na^+), potassium (K^+), and other ions (Leak current, L), mainly calcium and chloride, flowing through the cell membrane. Every component of the cell is treated as an electrical element. The lipid bilayer is represented by a capacitance (C_m). Voltage-gated ion channels are represented by conductances (g_i, where i is the specific ion) that are both voltage- and time-dependent. I is an externally applied membrane current per unit area. The electrochemical gradients driving the flow of ions are included via the Nernst potentials of the ions (E_i). The variable of interest is the membrane potential (V_m). The simplest HH model describes the properties of an excitable cell by a set of four ordinary differential equations:

$$\frac{dV_m}{dt} = \frac{1}{C_m}(-\bar{g}_{\mathrm{K}} n^4 (V_m - E_K) - \bar{g}_{\mathrm{Na}} m^3 h (V_m - E_{Na}) - \bar{g}_l (V_m - E_l) + I), \tag{1}$$

$$\frac{dn}{dt} = \alpha_n (V_m)(1-n) - \beta_n (V_m) n, \tag{2}$$

$$\frac{dm}{dt} = \alpha_m (V_m)(1-m) - \beta_m (V_m) m, \tag{3}$$

$$\frac{dh}{dt} = \alpha_h (V_m)(1-h) - \beta_h (V_m) h, \tag{4}$$

where α_i and β_i are rate constants for the i-th ion channel. These depend on voltage but not on time. To obtain conductances, the maximal conductances $\bar{g}_i$ are multiplied with $a^c b^d$, where a and b are dimensionless gating variables of ion channels. The variables used here are n, m, h, associated with respectively potassium activation, sodium activation, and sodium inactivation. c and d are integers. The sodium current is transient since the corresponding channel contains both activation and inactivation gates. The potassium current is persistent since the channels do not have inactivation gates. Expressions for the rate constants can be fitted to experimental data. The HH model can simulate APs. If a constant current input I exceeds a specific threshold current, I_{th} or *rheobase*, the neuron will start to spike. If the input current increases, the frequency of the spikes will increase. An example is shown in Figure 2.

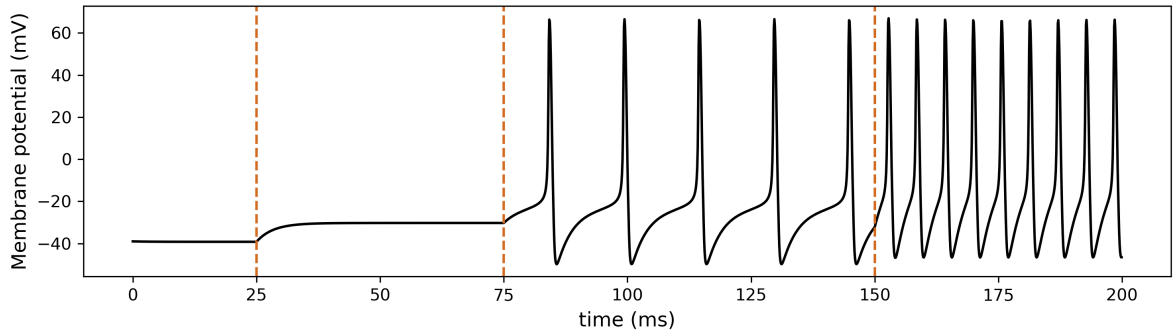

Figure 2: Dynamics of the Hodgkin-Huxley neuron model. Between $t = 0$ and $t = 25$ ms, no external input current I is applied. The neuron is at rest. At $t = 25$ ms, a continuous input current of 8 pA is applied. Since $I < I_{th}$, the membrane potential settles at a new resting potential. At $t = 75$ ms, $I = 25$ pA, which is slightly higher than I_{th}, therefore APs are generated. When I is raised to 35 pA at $t = 150$ ms, the AP frequency increases.

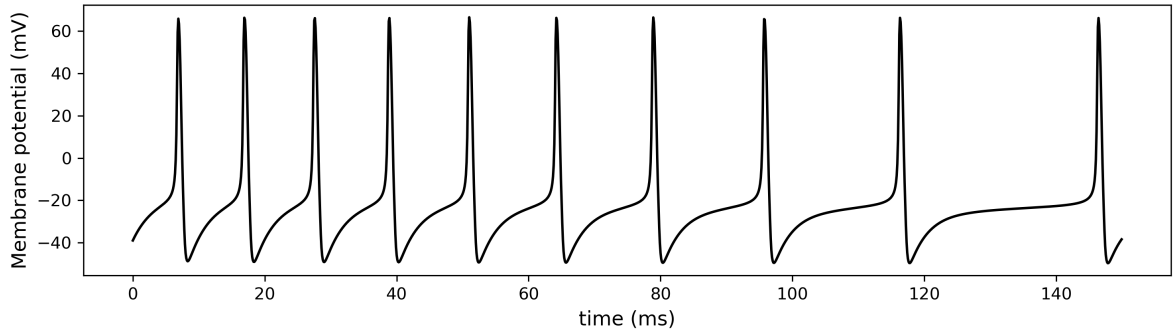

Figure 3: Hodgkin-Huxley neuron showing spike-frequency adaptation in response to a continuous external input current. As the current input persists, the interval between subsequent spikes grows and thus the frequency of the spikes lowers.

Synaptic plasticity and spike-frequency adaptation

From previous computational modeling of spontaneous network activity of cultured neuronal networks [19, 21, 22, 57, 58], it becomes apparent that a few mechanisms are necessary to model NB activity as observed from the MEA recordings.

An important mechanism to generate spontaneous synchrony is spike-frequency adaptation, especially in networks of purely excitatory neurons [21, 57]. Spike-frequency adaptation is the phenomenon that neurons show a reduction in firing frequency when stimulated with a constant current [59]. An example is shown in Figure 3. Several possible biophysical mechanisms can cause spike-frequency adaptation. They can be divided into two categories. The first is the inactivation of depolarizing currents. Sodium channels responsible for AP generation inactivate in response to depolarization and then recover slowly. This ensures that after a spike, fewer sodium channels are available for AP generation. This causes the delay to the next spike to increase. The second category is activity dependent activation of slow hyperpolarizing currents. The activity can either be voltage or spike dependent. An example of a voltage-dependent hyperpolarizing current is the non-inactivation potassium current I_M. Examples of spike dependent hyperpolarizing currents are the calcium-activated potassium current or the after-hyperpolarizing current I_{AHP}. These currents are activated by an increase in calcium concentration in the cell due to calcium influx at the peak of an AP. Neurons can have several adaptation processes with different time constants [59]. However, it is not easily determined what mechanisms are at play in the neurons we try to model. One might choose to model one of the mechanisms that sufficiently recreates the effects of spike-frequency adaptation observed in experiments.

Masquelier and Deco [21] and Park et al. [20] demonstrated the importance of short-term synaptic plasticity in obtaining the correct NB characteristics in simulations of neuronal networks. Synaptic plasticity [60] means that the synaptic strength, the amplitude of the post-synaptic potentials (PSPs), can vary over time and depends on previous activity. There are different mechanisms of synaptic plasticity, each with their own time frame. Synapses can experience both potentiation and depression. We usually differentiate between short-term- and long-term plasticity. Since we are not interested in large structural network changes over time in this study, we will not further discuss long-term plasticity. Short-term plasticity can last for a few minutes at maximum and includes facilitation (STF) and depression (STD). STF arises because the calcium concentration in the presynaptic neuron increases, increasing the synaptic vesicles' ability to fuse with the membrane. STD is caused by depletion of the readily available synaptic vesicles [60]. Markram and Tsodysk [61] showed that at synapses between excitatory neurons, only short-term depression is at play.

3 | Methods

3.1 Experimental data

Experimental data is provided by the group of dr. N. Nadif Kasri. hiPSC lines [8] were obtained by reprogramming skin fibroblasts (WT) or leukocytes (GEFS+ and DS), and they were differentiated into upper layer excitatory cortical neurons. About 20.000 neurons were co-cultured with 20.000 rodent astrocytes per well. Spontaneous network activity was recorded using multiwell-MEAs consisting of 24 individual wells (Multichannel systems, MCS GmbH, Reutlingen, Germany). Each well has 12 electrodes with a diameter of 30 μm, spaced 300 μm apart. The activity of the networks was recorded for 10 minutes in a recording chamber maintained at a constant 37 °C/95% O_2/5% CO_2. The neurons were cultured for 37 DIV (Days In Vitro) when measurements were taken.

3.2 Model components

The model consists of biologically realistic neurons, connected via plastic synapses into a network. The model is made up of several existing submodels that turned out to be critical for the generation of realistic network bursting behavior in previous research. Neuron, synapse, and network parameter values are based on literature where possible. We calibrate the remaining parameters to experimental data using an empirical parameter search.

3.2.1 Neuron model

We use a HH type neuron model as explained in section 2.3.2. Expressions for the rate constants well suited for cortical pyramidal cells are used, adapted to experimentally observed single-cell electrophysiology by [62]:

$$\alpha_m = \frac{-0.32\,(V_m - V_T - 13)}{\exp\left[-\left(V_m - V_T - 13\right)/4\right] - 1}, \tag{5}$$

$$\beta_m = \frac{0.28\,(V_m - V_T - 40)}{\exp\left[\left(V - V_T - 40\right)/5\right] - 1}, \tag{6}$$

$$\alpha_h = 0.128 \exp\left[-\left(V_m - V_T - 17\right)/18\right], \tag{7}$$

$$\beta_h = \frac{4}{1 + \exp\left[-\left(V_m - V_T - 40\right)/5\right]}, \tag{8}$$

$$\alpha_n = \frac{-0.032\,(V_m - V_T - 15)}{\exp\left[-\left(V_m - V_T - 15\right)/5\right] - 1}, \tag{9}$$

$$\beta_n = 0.5 \exp\left[-\left(V_m - V_T - 10\right)/40\right]. \tag{10}$$

We introduce V_T to allow for adjusting the spike threshold to our experimental data. Maximal conductances are also taken from [62]. Nernst potentials and V_T are adapted such that the simulated neurons have the same resting membrane potential, spike threshold potential, and AP amplitude as our *in vitro* neurons. All parameter values can be found in Table 1.

Adaptation model
We include spike-frequency adaptation in every neuron in the form of an additional after-hyperpolarization current I_{AHP}, given by:

$$I_{AHP} = g_{AHP}(V_m - E_K). \tag{11}$$

The current is modeled as a potassium current driven by an increase of the calcium concentration inside the neuron. The calcium concentration in the neuron increases when an AP is fired. g_{AHP} is the accompanying conductance, which is initially zero. When a spike occurs, the conductance increases with α_{Ca}.

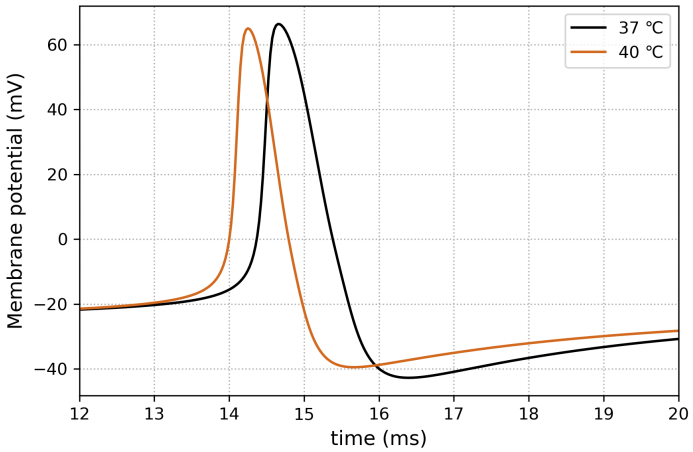

Figure 4: Change of the shape of the AP in response to a temperature increase from 37°C (black line) to 40°C (orange line) of a neuron with a constant current input $I = 14$ pA. For the higher temperature, the amplitude of the AP is slightly decreased and the duration of the AP is reduced.

The conductance then decays back to zero with time constant τ_{AHP}. The resulting equation for the conductance is:

$$\frac{dg_{AHP}}{dt} = -\frac{g_{AHP}}{\tau_{AHP}} + \alpha_{Ca}\delta(t - t_0), \tag{12}$$

where $\delta(t - t_0)$ is zero for $t \neq t_0$ and otherwise 1. This models only a calcium-activated potassium current, but the effect can also correspond to other fatigue mechanisms such as those explained in section 2.3.2. τ_{AHP} is the apparent recovery timescale of all these mechanisms combined, which is chosen in the 2-8s range found in literature [21]. Parameters for the WT model can be found in Table 1.

Noise and heterogeneity

To induce spontaneous activity in the neurons, we induce voltage fluctuations in every neuron, using:

$$V_{noise} = \sigma\sqrt{g_l C_m}\xi, \tag{13}$$

where ξ is Gaussian white noise with mean zero and σ is the standard deviation of the resulting noise in the membrane potential. This noise can mimic synaptic or membrane noise.

Besides noise, we need to add more heterogeneity to the neurons since heterogeneous cell properties are proven to be crucial to obtain non-periodic synchronization of neurons as seen in cultures [63]. We model this in the form of a continuous externally applied current I with amplitudes drawn from a uniform distribution between -9.5 and 9.5 pA. This is to account for the biological differences between neurons. Because of the difference in externally applied current, some neurons are more excitable than others.

Temperature dependency

We include temperature dependency in the neuron model to eventually validate the models of GEFS+ and DS. Hodgkin and Huxley assumed that only the rates of change of the conductance gating variables depend on temperature [56]. To model this, we multiply these rates of change by a factor ϕ:

$$\phi = 3^{(T-37)/10}, \tag{14}$$

where T is the temperature in degrees Celsius. The effect of temperature increase on the AP of the neuron resulting from a constant current input can be seen in Figure 4. We can see the amplitude and duration of the AP are reduced as temperature increases, which is in line with literature [64].

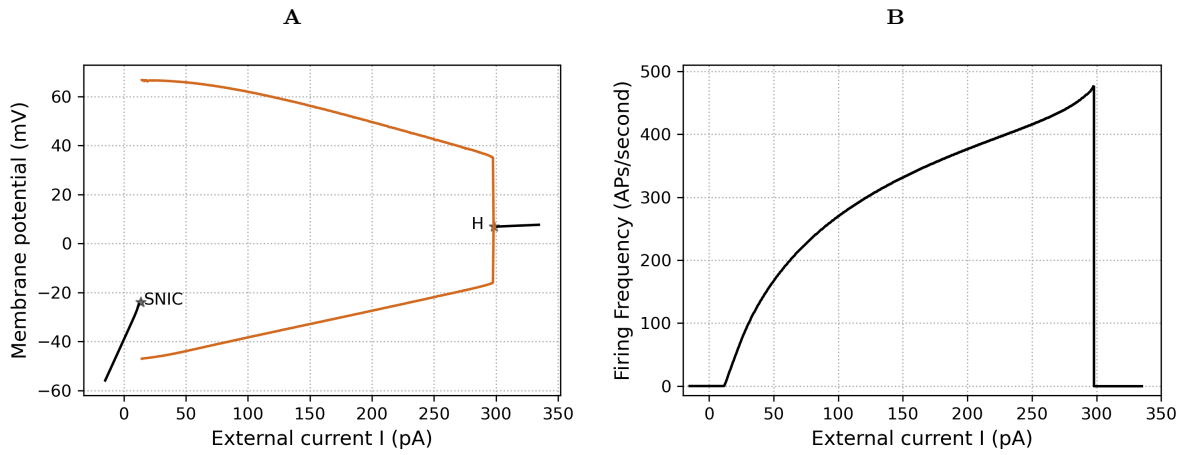

Figure 5: Dynamics of the neuron model. **A**. Simplified bifurcation diagram only showing stable equilibria. The black lines denote a stable fixed point. The orange lines denote the maximum and minimum values of V_m at the stable limit cycle. At the SNIC (Saddle-Node on an Invariant Circle) bifurcation, an undrawn saddle point collides with the stable fixed point, and both disappear. Because these fixed points were on an invariant circle, their collision gives rise to a stable limit cycle. At H, a supercritical Hopf bifurcation (Lyapunov coefficient = -4.24e-3) occurs, leading to a depolarization block. The stable limit cycle collides with an undrawn unstable fixed point that then becomes a stable fixed point. **B**. I-F curve of the neuron model. The neuron starts firing when I exceeds the threshold I_{th}=13 pA. The neuron stops firing when the depolarization block is reached at I=300 pA.

Thus, the resulting neuron equations are:

$$\frac{dV_m}{dt} = \frac{1}{C_m}(-\bar{g}_{\mathrm{K}} n^4 (V_m - E_K) - \bar{g}_{\mathrm{Na}} m^3 h (V_m - E_{Na}) - \bar{g}_l (V_m - E_l) + I + I_{AHP}+) + V_{noise}, \quad (15)$$

$$\frac{dn}{dt} = \phi(\alpha_n (V_m)(1-n) - \beta_n (V_m) n), \quad (16)$$

$$\frac{dm}{dt} = \phi(\alpha_m (V_m)(1-m) - \beta_m (V_m) m), \quad (17)$$

$$\frac{dh}{dt} = \phi(\alpha_h (V_m)(1-h) - \beta_h (V_m) h). \quad (18)$$

Figure 5 shows the simplified bifurcation diagram and current-frequency (I-F) curve of this model neuron at 37°C without noise. We can see in the bifurcation diagram that the radius of the stable limit cycle does not appear to slowly decrease to 0 at the Hopf bifurcation. This is due to the spike-frequency adaptation. It keeps the neuron from reaching a depolarization block at high input currents, and then suddenly, a bifurcation point is reached. A bifurcation diagram without the spike-frequency adaptation current can be found in Appendix A.

3.2.2 Synapses and plasticity

Since all *in vitro* neurons are excitatory, we only model glutamatergic synapses. Excitatory postsynaptic currents (EPSCs) have both AMPA and NMDA components. We add a synaptic current I_{syn} to the HH equations:

$$I_{syn}(t) = I_{AMPA}(t) + I_{NMDA}(t). \quad (19)$$

AMPA-type glutamate receptors display an approximately linear current-voltage relationship when they open. Therefore, they can be modeled as an ohmic conductance g_{AMPA} multiplied with the difference between the membrane potential V_m of the post-synaptic neuron and the Nernst potential E_{AMPA} of the AMPA channels [65]. In contrast with AMPA-receptors, NMDA-receptor-mediated conductance also depends on the postsynaptic voltage. The voltage dependency is caused by blocking of the pore of the NMDA-receptor from the outside by a magnesium ion. At resting potential, the channel is nearly completely blocked. When the cell depolarizes, the magnesium block is lifted. The fraction of channels

that are not blocked by magnesium can be fitted to:

$$u(V_m) = \frac{1}{1 + e^{-aV_m}[Mg^{2+}]_o/b}, \tag{20}$$

where V_m is the membrane potential of the postsynaptic neuron and $[Mg^{2+}]_o$ is the extracellular magnesium concentration, which we simply take to be 1 mM [66]. We take $a = 0.062$ mV^{-1} and $b = 3.57$ mM [66]. We assume that the magnesium block changes instantaneously with voltage and is independent of the gating of the channel. The NMDA-receptor-mediated synaptic current is then modeled as the conductance multiplied with $u(V_m)$ and multiplied with the driving force. The conductances can be modeled as maximal conductances of all the AMPA and NMDA channels, $\bar{g}_{AMPA}$ and $\bar{g}_{NMDA}$ respectively, times the fraction of open AMPA and NMDA channels. The fraction of open NMDA channels is the sum of the fractions of open channels per synapse with pre-synaptic neuron j, s_j^{NMDA}, multiplied with the synaptic weight from pre-synaptic neuron j to the post-synaptic neuron w_j. The equations for both synaptic currents are thus given by:

$$I_{AMPA} = \bar{g}_{AMPA}(V_m - E_{AMPA}) \sum_{j=1}^{N_E} w_j s_j^{AMPA}, \tag{21}$$

$$I_{NMDA} = \bar{g}_{NMDA} u(V_m)(V_m - E_{NMDA}) \sum_{j=1}^{N_E} w_j s_j^{NMDA}. \tag{22}$$

The fraction of open channels is given by:

$$\frac{ds_j^{AMPA}}{dt} = -\frac{s_j^{AMPA}}{\tau_{AMPA}} + \sum_k \delta(t - t_j^k - \Delta), \tag{23}$$

$$\frac{ds_j^{NMDA}}{dt} = -\frac{s_j^{NMDA}}{\tau_{NMDA,decay}} + \alpha_{NMDA} x_j^{NMDA}(1 - s_j^{NMDA}), \tag{24}$$

$$\frac{dx_j^{NMDA}}{dt} = -\frac{x_j^{NMDA}}{\tau_{NMDA,rise}} + \sum_k \delta(t - t_j^k - \Delta). \tag{25}$$

Here, x_j^{NMDA} is an auxiliary gating variable for NMDA, and α_{NMDA} is a multiplicative constant. The fraction of open channels gets increased every time the pre-synaptic neuron spikes at time t_j^k; therefore, we sum over all these spikes. $\tau_{NMDA,rise}$ and $\tau_{NMDA,decay}$ are the rise and decay times for the NMDA synapses and τ_{AMPA} the decay time for AMPA synapses. These equations and the values for the time constants are taken from [21]. We neglect the AMPA rise time because it is very short [21]. Δ is a homogeneous conduction delay which we will further explain in section 3.2.3. The values of the parameters can be found in Table 1. We choose the values of the maximal conductances such that the AMPA:NMDA current ratio matches experimental observations. Figure 6 shows the different time courses of AMPA and NMDA synaptic currents.

Short-Term Depression

All synapses are modulated by STD. We use the phenomenological model proposed by Markram and Tsodysk [61]. The model is based on the concept of synaptic resources, of which only a fraction, x, is available. The synaptic weight w_j is multiplied with x_j, where x_j obeys:

$$\frac{dx_j}{dt} = \frac{1 - x_j}{\tau_D} - U x_j \sum_k \delta(t - t_j^k - \Delta), \tag{26}$$

where τ_D is the time constant of STD, which value Markram and Tsodysk determined for excitatory synapses to be 813 ms. U is the strength of STD, set to U = 0.015, which is in the biological range also measured by Markram and Tsodysk [61].

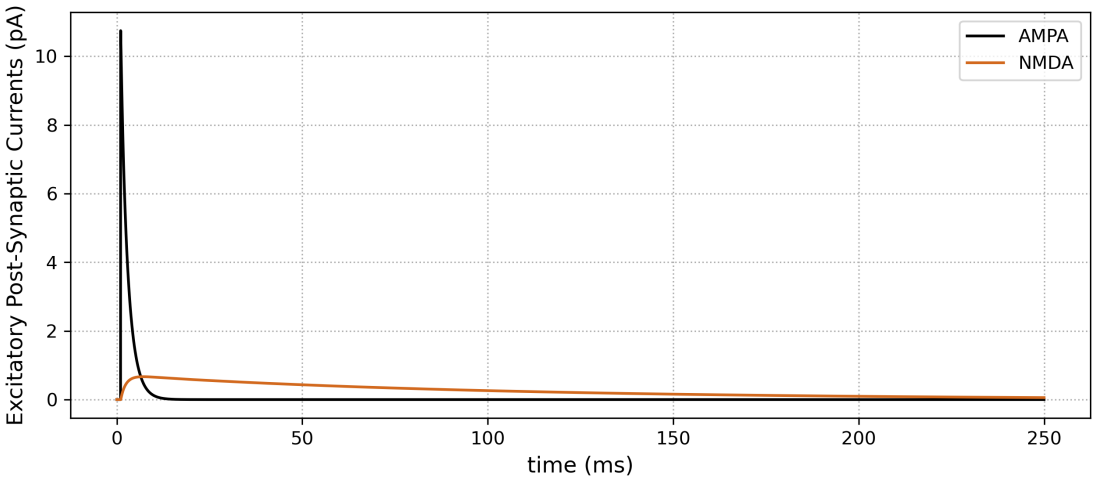

Figure 6: Excitatory Post-Synaptic Currents (EPSCs) after the arrival of one pre-synaptic spike at t = 1 ms. The AMPA EPSC rises instantaneously and decays fast. The NMDA EPSC rises relatively slow and decays even slower.

3.2.3 Network properties

We use a sparsely connected network of $N = 100$ neurons. We randomly connect all neurons to a subset of other neurons with a connection probability of 30%. This means every neuron is connected to about 30 other neurons. Different numbers of neurons (N = 50-10.000) and different types of connectivity were explored (full connectivity, small-world topology, and distance-dependent connectivity), the methods and outcomes can be found in Appendix B.

Previous simulations showed that non-homogeneous weights are necessary to obtain realistic bursting behavior [15]. Therefore, we take synaptic weights w_{ij} from a normal distribution with a mean of 1 and a standard deviation of 0.7. We set values below 0 to 0, and values above 2 to 2. This causes about 1 in 15 synapses to be 0, and thus these synapses perish.

The conduction delay Δ_{ij} of the synapse from neurons i to j is determined by the euclidean distance between these neurons. We place all neurons on a square grid of 10 times 10 neurons. We give every neuron an x and y coordinate based on their place in the grid and the grid distance d_{grid}. We set this distance to 45 micrometer, which is the average distance between neurons *in vitro*. We assume the maximal conduction delay Δ_{max} between two neurons is 25 ms, as was measured in cultured neuronal networks [67]. We determine the conduction velocity, v by dividing the maximal distance between neurons in the model by the maximal delay:

$$v = \frac{\sqrt{10^2 + 10^2} d_{grid}}{\Delta_{max}}. \tag{27}$$

The delay is then determined by dividing the Euclidean distance between the neurons by the conduction velocity:

$$\Delta_{ij} = \frac{\sqrt{(x_i - x_j)^2 + (y_i - y_j)^2}}{v}. \tag{28}$$

3.3 Model validation

To validate the model, an experimental intervention is performed on the cultures by the group of dr. N. Nadif Kasri. We perform the same intervention in the model, and we compare the effect. As experimental intervention, AMPA and NMDA-receptors are blocked. AMPA-receptors are blocked using NBQX and hydrochloride. NMDA-receptors are blocked using Dizocilpine. An 8 well setup is used, where the basal behavior is recorded for 10 minutes, followed by adding the hydrochloride and NBQX to four wells and Dizocilpine to the remaining four wells. After 10 minutes, another 10-minute recording is made. In

the simulation, we model this by simulating a basal network for 10 minutes, then keeping the random number realizations the same as we subsequently remove the AMPA and NMDA currents, I_{AMPA} and I_{NMDA}, from all the neurons, and simulate for 10 minutes.

3.4 Modeling GEFS+ and DS

3.4.1 Modification of the voltage-gated sodium channel

To model the hypothesized changes in the voltage-gated sodium channel functioning, we use a modification of the HH model that permits alteration of the activation, inactivation, conductance, and voltage sensitivity of the sodium channel. Moreover, since our HH model does not differentiate between fast and slow inactivation, we model the change to a persistent sodium current differently. We add a separate persistent sodium current, with infinitely fast activation m_∞ and slow inactivation h_p. The parameters γ_{Na}, γ_{Nap}, $\gamma_{\tau m}$, $\gamma_{\tau h}$, $\gamma_{\alpha m}$, $\gamma_{\alpha h}$, $\gamma_{\beta m}$, $\gamma_{\beta h}$, ΔV_m and ΔV_h are incorporated into the HH equations:

$$\frac{dV_m}{dt} = \frac{1}{C_m}(-\bar{g}_{\mathrm{K}} n^4 (V_m - E_K) - \gamma_{Na}(1-\gamma_{Nap})\bar{g}_{\mathrm{Na}} m^3 h (V_m - E_{Na}) - \bar{g}_l (V_m - E_l) \tag{29}$$

$$+ \gamma_{Nap}\bar{g}_{\mathrm{Nap}} m_\infty h_p (V_m - E_{Na}) + I + I_{AHP}) + V_{noise}, \tag{30}$$

$$\frac{dn}{dt} = \phi(\alpha_n (V_m)(1-n) - \beta_n (V_m) n), \tag{31}$$

$$\frac{dm}{dt} = \phi\gamma_{\tau m}(\gamma_{\alpha m}\alpha_m (V_m - \Delta V_m)(1-m) - \gamma_{\beta m}\beta_m (V_m - \Delta V_m) m), \tag{32}$$

$$\frac{dh}{dt} = \phi\gamma_{\tau h}(\gamma_{\alpha h}\alpha_h (V_m - \Delta V_h)(1-h) - \gamma_{\beta h}\beta_h (V_m - \Delta V_h) h), \tag{33}$$

$$\frac{dh_p}{dt} = \phi(\alpha_h (V_m)(1-h_p) - \frac{4}{1+\exp[(V_m - V_T - 40)/5]} h_p), \tag{34}$$

where γ_{Na} modulates the maximum conductance of the sodium channels, which is analogous to altering the expression levels of the channel. Increasing γ_{Nap} above 0, will result in a shift to a persistent sodium current. $\gamma_{\tau m}$ and $\gamma_{\tau h}$ scale both rate constants α and β with the same factor so that effectively, the time constants, $\tau_i = \frac{1}{\alpha_i(V_m)+\beta_i(V_m)}$ of the $i = m$ and $i = h$ gate respectively, are scaled by $1/\gamma_{\tau i}$, while leaving the steady state, $i_\infty = \frac{\alpha_i(V_m)}{\alpha_i(V_m)+\beta_i(V_m)}$ unaffected. The kinetics of the sodium channel are also modified by altering the rates of activation and deactivation of both the m and h gate individually using $\gamma_{\alpha m}$, $\gamma_{\alpha h}$, $\gamma_{\beta m}$ and $\gamma_{\beta h}$, leading to changes in both time constants and steady-states. The parameters ΔV_m and ΔV_h simultaneously shift the voltage sensitivity of both rate constants of the m and h gate respectively. $\Delta V_i > 0$ corresponds to a depolarizing shift in the voltage dependency and $\Delta V_i < 0$ to a hyperpolarizing shift. The WT sodium channel model has parameter values $\gamma_{Na} = \gamma_{\tau m} = \gamma_{\tau h} = \gamma_{\alpha m} = \gamma_{\alpha h} = \gamma_{\beta m} = \gamma_{\beta h} = 1$ and $\gamma_{Nap} = \Delta V_m = \Delta V_h = 0$.

Since we have 10 parameters to modify the sodium channel functioning, it is not computationally feasible to explore the entire parameter space. This may also be unnecessary since it is biologically unlikely that more than two parameters are altered simultaneously. Only Volkers et al. [39] found a mutation that resulted in changes that should be modeled by three of these parameters, but one of the effects was very small compared to the other two. Therefore, we only look at changes in single parameters or combinations of two parameters. First, we explore changes in single parameters and determine the step size for a more extensive parameter space exploration with combinations of 2 parameters.

Besides changes in the dynamics of the voltage-gated sodium channel, network parameters might also change. The synaptic strengths might change; therefore, we incorporate a scaling factor S, with which all synaptic weights w are multiplied.

3.4.2 GEFS+ and DS model validation

To validate the GEFS+ model and the DS model, we again use an experimental intervention. As GEFS+ and DS are both often associated with febrile seizures, we suspect the response of the GEFS+ and DS cultures to temperature increase will be different from WT cultures. Thus, the temperature of the three cultures is increased from 37 °C to 40 °C. We do the same in the model and compare the effect. Temperature is included in the model as described in section 3.2.1.

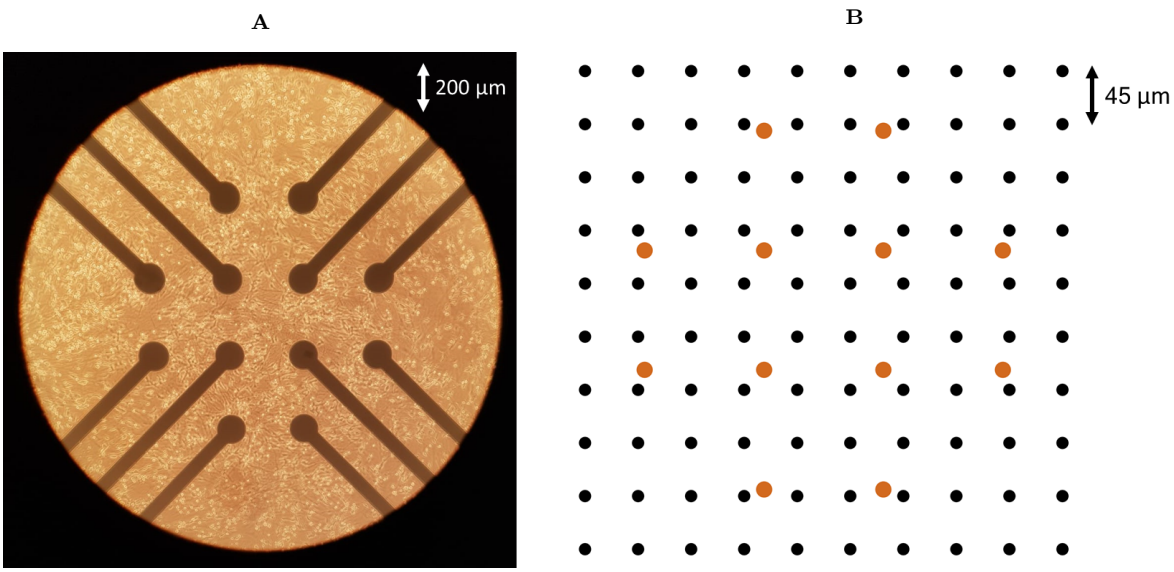

Figure 7: **A**. Photo of the electrodes in a Multiwell-MEA well with cultured neurons in our lab. **B**. Positions of the virtual electrodes (orange dots) in the grid of 100 neurons (black dots) of the model.

3.5 Simulations

We made custom Python 3.6 code for the Brian 2 simulator [68]. The differential equations of the neurons are integrated numerically using the Exponential Euler method. The synapse equations are integrated using the Euler Forward method. Both use a 100 µ*s*-time step, which is the same as the sample time of the MEA recordings. The code can be found on `https://github.com/Ninontwik/Master_Thesis_final.git`.

3.6 Data analysis

To optimally compare simulation and experiment, we first have to obtain a model output similar to the experimental recordings. Next, we have to define output measures that give a defined description of the network behavior and differences in behavior between WT, GEFS+ and DS networks.

3.6.1 Model output

To mimic the signal measured from the *in vitro* neuronal networks with the MEAs, we model virtual electrodes. We define 12 electrodes with positions with the same arrangement as the multi-well MEA set up, as can be seen in Figure 7. Every electrode measures a weighted sum of the membrane potential of the surrounding neurons. The signal measured by the electrodes is computed as follows:

$$V_{elec} = \sum_{i=1}^{N} \frac{V_{m,i}}{D\sqrt{(x_{elec} - x_i)^2 - (y_{elec} - y_i)^2}}, \tag{35}$$

where D scales the distance dependence. We take D such that every electrode measures voltage from about 10 surrounding neurons. The output of a simulation is the signal from the 12 virtual electrodes.

3.6.2 Output measures

The signal measured *in vitro* with the MEAs, and the virtual electrode signal from the model, are handled in the same manner. To obtain signals containing APs, signals are filtered between 100 and 3500 Hz using a Butterworth filter [8]. We detect APs using an amplitude threshold-based method. The threshold is determined for every electrode; we set it to four times the root mean square of the signal [8]. In both simulations and experiments, the NBs have an all-or-nothing nature and are easy to detect based on the spike rate. We determine the spike rate at 20 millisecond time windows. The start of the NB is detected when the spike rate of three subsequent time windows is higher than a threshold (thr1).

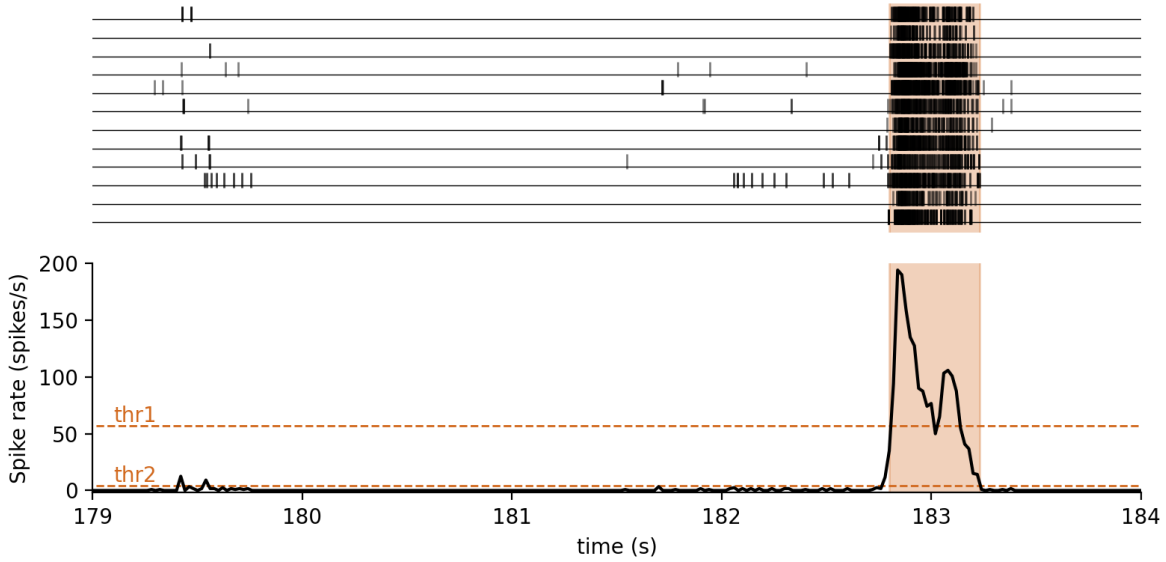

Figure 8: Illustration of NB detection. The orange rectangle spans the detected NB. Top: raster plot of spikes detected at the 12 electrodes. Bottom: NB detection based on the spike rate. The start of the NB is detected if the spike rate rises above thr1. The end of the NB is detected if the spike rate falls below thr2.

We set this threshold to be $\frac{1}{4}$th of the maximum spike rate of the signal. The end of the NB is detected when the spike rate falls below $\frac{1}{100}$th of the maximum spike rate (thr2). This is illustrated in Figure 8. To make sure the burst is a network burst, and does not consist of spikes at only one electrode, a check is performed. If the spike count of the entire burst is made up of more than 80% of spikes of a single electrode, the burst is excluded. We validate this method by visual inspection of the signals.

We define four output measures based on the most notable differences between the signals measured from WT, GEFS+ and DS cultures. These are:

- the Mean Network Burst Rate (**MNBR**), the average amount of NBs per minute,
- the Mean Network Burst Duration (**MNBD**), the mean time difference between the start and the end of the NBs in seconds,
- the Percentage of Spikes In Burst (**PSIB**), which is the $\frac{\#\text{ of spikes in NBs}}{\#\text{ of spikes outside NBs}}100\%$,
- **ElecSD**, which is the mean standard deviation of the fractions of spike counts every electrode contributes to NBs. If this number is 0, every electrode contributes the same amount of spikes to the NBs. A high number means the spikes in the NBs come more from some electrodes than others. In other words, ElecSD provides a measure for in-burst activity similarity between electrodes.

All measures are computed over 10 minutes (600 seconds) of measurement.

3.6.3 Statistical analysis

From *in vitro* experiments, we have 600-second measurements from 12 different wells per culture type. To mimic the different wells with the model, we model 12 networks with different random number realizations. This results in 12 networks with different random connectivity, different synaptic weights w, and different externally applied currents I. Networks are simulated for 600 seconds each.

We perform statistical analysis using the SciPy statistical functions module in Python 3.6. We ensure normal distributions using a Shapiro-Wilk Test. Equal variances of the to-be-compared groups are ensured using Levene's test. When comparing three groups (WT, GEFS+ and DS) with equal variances, we perform a one-way ANOVA and post-hoc Tukey HSD test. If variances are not equal, we perform a one-way ANOVA with Welch correction and post-hoc Games-Howell test. When comparing experiment to simulation, a Welch's t-test is performed. p-values$<$0.05 are considered significant in all cases.

Table 1: Overview of WT model parameters.

Parameter	Description	Value	Unit
C_m	Membrane Capacitance	1	μF·cm^{-2}
$\bar{g}_{\mathrm{K}}$	Maximum voltage-gated potassium conductance	5	mS·cm^{-2}
$\bar{g}_{\mathrm{Na}}$	Maximum voltage-gated sodium conductance	50	mS·cm^{-2}
$\bar{g}_l$	Leak conductance	0.3	mS·cm^{-2}
E_K	Nernst potential of potassium	-80	mV
E_{Na}	Nernst potential of sodium	70	mV
E_l	Nernst potential of the leak current	-39.2	mV
V_T	Potential to adapt spike threshold	-30.4	mV
α_{Ca}	Strength of spike-frequency adaptation (SFA)	0.0035	nS
τ_{AHP}	Apparent recovery timescale of all SFA mechanisms	6	s
σ	Standard deviation of the noisy input	4.1	mV
$\bar{g}_{AMPA}$	Maximal conductance of AMPA	0.2808	nS
$\bar{g}_{NMDA}$	Maximal conductance of NMDA	0.0981	nS
E_{AMPA}	Nernst potential of AMPA	0	mV
E_{NMDA}	Nernst potential of NMDA	0	mV
α_{NMDA}	Multiplicative constant of NMDA dynamics	0.5	kHz
τ_{AMPA}	Decay time for AMPA synapses	2	ms
$\tau_{NMDA,decay}$	Decay time for NMDA synapses	100	ms
$\tau_{NMDA,rise}$	Rise time for NMDA synapses	2	ms
$\bar{g}_{\mathrm{Nap}}$	Maximal persistent sodium conductance	0.1	mS·cm^{-2}

4 | Results

4.1 Experimental results

The experimental results are shown in Figure 9. We can see distinct differences in output measures between WT, GEFS+, and DS. For MNBR, there is a significant difference between all three groups. The MNBD is significantly higher in DS cultures, compared to WT and GEFS+. The PSIB is significantly lower in both GEFS+ and DS, compared to WT. The ElecSD is significantly higher in both GEFS+ and DS, compared to WT.

4.2 Model results

4.2.1 WT model

The results of the WT model are shown in Figure 10. There are no significant differences between MNBR and MNBD of experiment and simulation. There is, however, a significant difference in PSIB and ElecSD. The fraction difference between the means of the PSIB of experiment and simulation is only 4%. We see that the variances of the output measures of simulations are smaller than those of experiments.

4.2.2 Model validation

The results of the model validation are shown in Figure 11. When blocking the NMDA receptors *in vitro*, we only see a significant change in the MNBD. As can be seen from the boxplot, the same happens in simulations. There is no significant difference in normalized MNBD between experiment and simulation, although the simulation observations have a more narrow distribution. As in experiments, there is also no significant change in MNBR, PSIB, and ElecSD in the simulations when the NMDA receptors are blocked. When the AMPA receptors are blocked, all bursting behavior vanished in both experiment and simulations in all cases.

4.2.3 GEFS+ and DS models

To obtain a model of GEFS+ and DS, we first explored the effect of single modification parameters as described in section 3.4.1. We observed that every parameter either increased or decreased neuron excitability and that this effect was roughly linear, meaning that if an increase of a parameter increased excitability, increasing it further increased excitability more, and decreasing it decreased excitability. For every parameter, we defined if increasing its value resulted in increased or decreased excitability and the parameter range for which this effect was stable. The result can be seen in Table 2. Because of the roughly linear effect of the modification parameters, we chose a large step size for parameter space exploration. The parameters γ_{Na}, $\gamma_{\tau m}$, $\gamma_{\tau h}$, $\gamma_{\alpha m}$, $\gamma_{\alpha h}$, $\gamma_{\beta m}$ $\gamma_{\beta h}$ were explored for the values 0.5, 0.75, 1, 1.25 and 1.5. γ_{Nap} was explored for values 0, 0.1 and 0.2. ΔV_m and ΔV_h were explored for values -5 mV, -2 mV, 0 mV, 2 mV and 5 mV. The effect on the network behavior of changing one or combinations of two parameters was observed. We found that parameter changes leading to increased neuron excitability always led to a higher MNBR, and parameter changes leading to decreased neuron excitability always led to lower MNBR. Changes of 2 parameters always had the sum of the individual effect qualitatively. So if parameters 1 and 2 both increased MNBR, changing both parameters simultaneously increased the MNBR even more. We observe lower MNBR in GEFS+ and DS cultures, but also lower PSIB and higher ElecSD. In simulations, the PSIB never dropped below 96.68%, and the ElecSD never significantly increased when only varying the modification parameters. Thus, changing the dynamics of the sodium channel alone does not result in the experimentally observed behavior. We also varied the weight scaling parameter S and found that decreasing it resulted in lower PSIB. Decreasing S, however, also led to lower MNBDs, which is not seen in GEFS+ and DS cultures. This effect can be counteracted by suppressing the adaptive mechanisms (spike-frequency adaptation and STD). Thus, increasing neuron excitability, decreasing S, and decreasing the adaptive mechanisms resulted in network behavior similar to experimentally observed behavior of GEFS+ and DS networks.

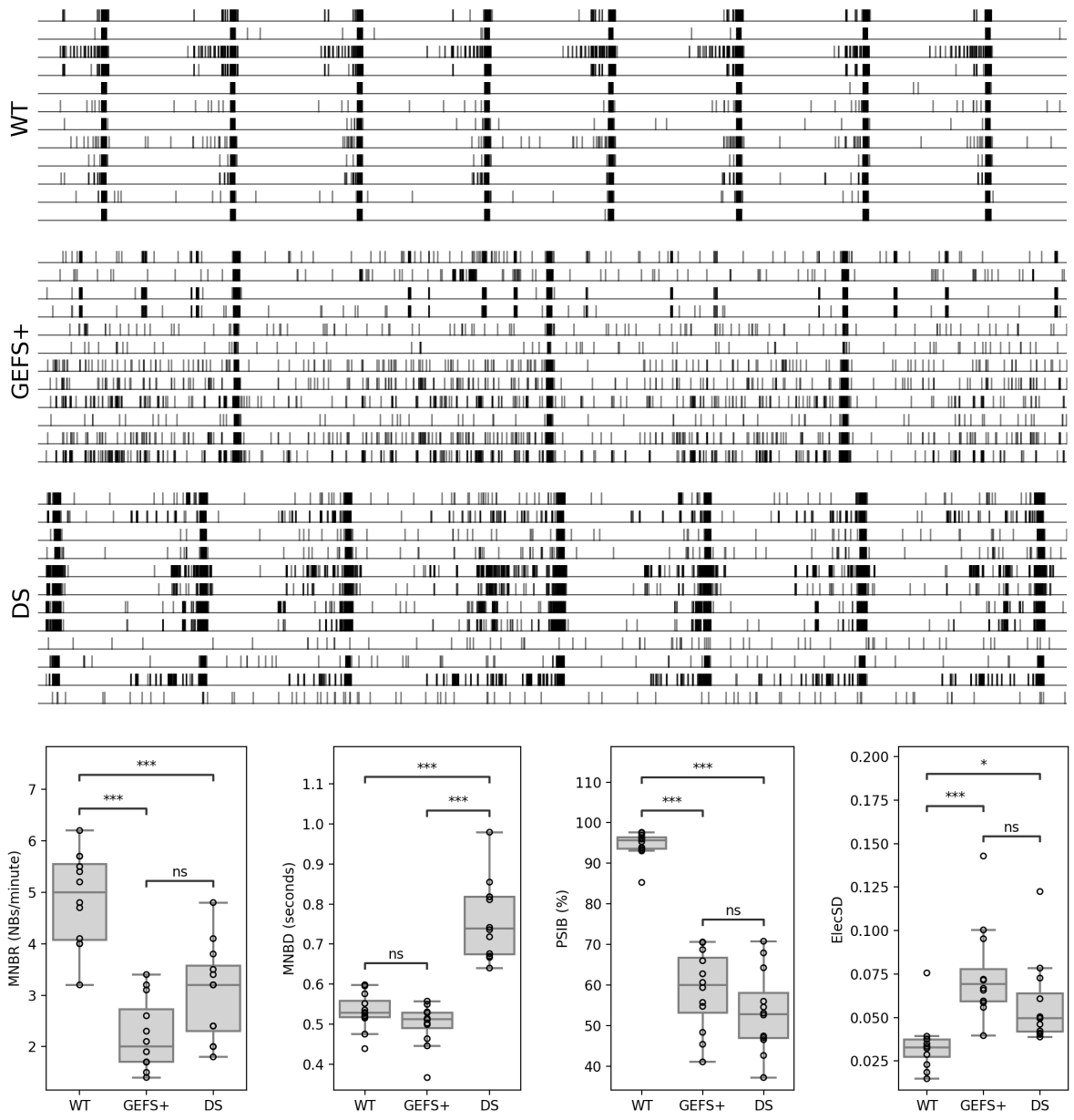

Figure 9: Comparison of WT, GEFS+ and DS spontaneous neuronal network activity in experiments. Top: representative raster plots of 120 seconds from WT, GEFS+ and DS cultures. Bottom: Box plots of output measures of the cultured neuronal networks. Per culture type (WT, GEFS+ and DS), 12 wells were recorded for 600 seconds each. Output measures for each well were calculated. ns $P>0.05$, * $P<0.05$, ** $P<0.01$, *** $P<0.001$, one-way ANOVA with post-hoc Tukey HSD was performed between culture types.

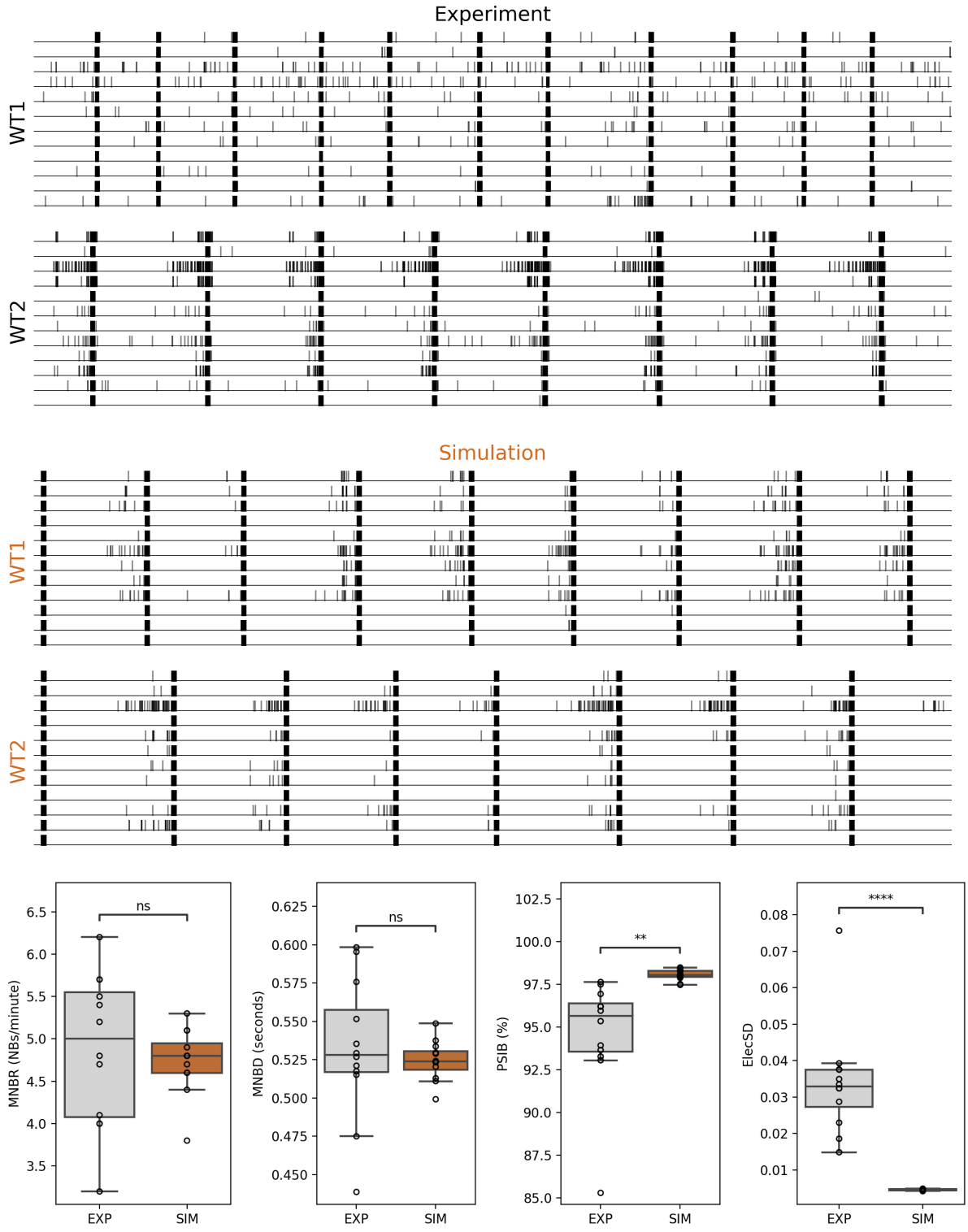

Figure 10: Comparison of WT behavior as observed from experiment (EXP) and simulations (SIM). Top: representative raster plots of 120 seconds from two wells of the experiment, and two simulations with different random number realisation. Bottom: boxplots of the output measures of 12 wells and 12 simulations. ns $P>0.05$, ** $P<0.01$, **** $P<0.0001$, Welch's t-test was performed between experiment and simulation.

Figure 11: Comparison of the effect of blocking of AMPA (AMPArb) and NMDA (NMDArb) receptors on network behavior between experiment (EXP) and simulations (SIM). Top: representative raster plots of 120 seconds from experiment and simulation. Bottom: Box plot showing the effect of NMDA receptor blocking on the MNBD in 4 wells in experiment and 4 simulations. ns P>0.05, a Welch's t-test was perfomed between experiment and simulation.

Table 2: Effect of increasing the values of the modification parameters on the neuron excitability. Increasing the parameter value (making it more positive) either increases (↑), decreases (↓), or does not influence (-) neuron excitability. The ranges for which the effect is stable are also given.

Parameter	Excitability	Stable range
γ_{Na}	↑	0.07 - 7.8
γ_{Nap}	↑	0 - 0.91
$\gamma_{\tau m}$	↑	0.18 - ∞
$\gamma_{\tau h}$	↑	0.001 - 6.2
$\gamma_{\alpha m}$	↑	0.35 - 9.3
$\gamma_{\alpha h}$	↑	0.04 - 7.9
$\gamma_{\beta m}$	↓	0.29 - 3.8
$\gamma_{\beta h}$	-	0.15 - 25
ΔV_m	↓	-13 - 6 mV
ΔV_h	↑	-15 - 23 mV

Table 3: Overview of parameters that were altered to obtain the model of GEFS+ and DS.

Parameter	Description	WT value	GEFS+ value	DS value
α_{Ca}	Strength of spike-frequency adaptation	0.0035	0.0025	0.001
S	Synaptic weight scaling factor	1.65	0.67	0.53
U	Strength of STD	0.015	0.007	0.0042
ΔV_m, ΔV_h	Shift of voltage dependence of the m- and h-gate	0 mV	-2 mV	0 mV
$\gamma_{\alpha m}$	Modifies activation rate of m-gate	1	1	1.5

Because multiple modification parameters can increase neuron excitability, several possibilities arise to model GEFS+ and DS networks. We know the genetic mutation of the GEFS+ patient is a missense mutation in the voltage sensing domain of the sodium channel. Therefore we choose to further analyze a GEFS+ model with a hyperpolarized shift in both activation and inactivation of the sodium channel. We keep in mind that this is just one option and that more possibilities can lead to roughly the same behavior. The DS patient has a missense mutation in the pore domain of the channel. We choose to further analyze a DS model where there is an increased rate of activation of the m-gate. The parameters we altered with respect to the WT model can be found in Table 3.

4.2.4 GEFS+

The results of the GEFS+ model are shown in Figure 12. There are no significant differences between MNBR and MNBD of experiment and simulation. There is a slight significant difference in PSIB. The simulations have a higher PSIB than is observed in experiments, as was also seen in the WT model. However, the PSIB of the simulations is significantly lower than that of WT simulations, which is in line with the experimentally observed difference between WT and GEFS+. There was a significant difference between ElecSD of experiment and simulations. There was no significant difference between ElecSD from the WT and GEFS+ simulations.

4.2.5 Dravet Syndrome

The results of the DS model are shown in Figure 13. There are no significant differences between MNBR and MNBD of experiment and simulation. There is a significant difference between PSIB and ElecSD of experiment and simulation. However, there is a significant decrease in PSIB of the DS simulation compared to the WT simulation. There is also a significant increase in ElecSD compared to the WT simulation. So PSIB and ElecSD follow the same trend in simulations as in the experiments.

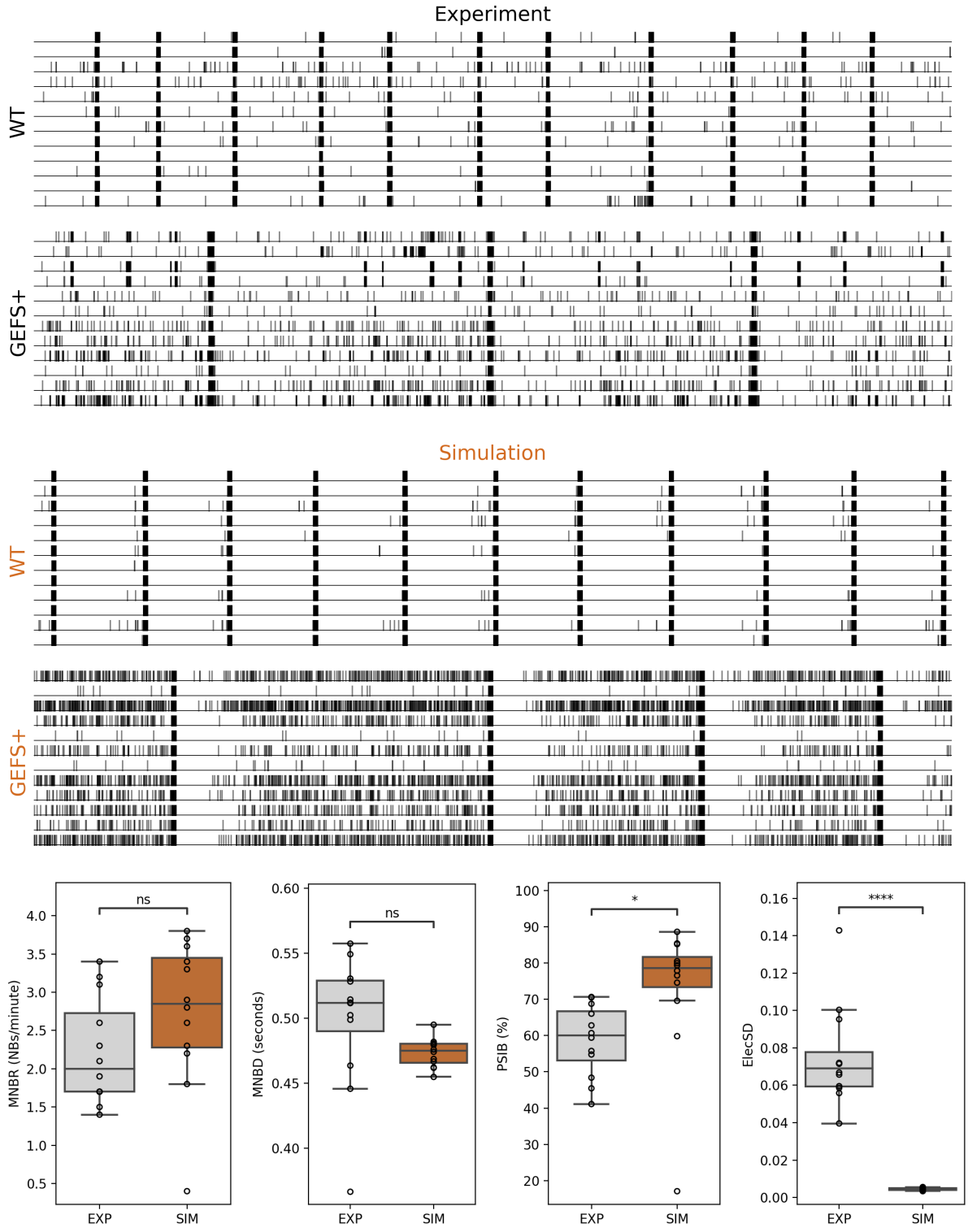

Figure 12: Comparison of GEFS+ behavior as observed from experiment (EXP) and simulations (SIM). Top: representative raster plots of 120 seconds from WT and GEFS+ of the experiment and simulations. Bottom: boxplots of the output measures of 12 wells and 12 simulations. ns P>0.05, * 0.01<P<0.05, **** P<0.0001, Welch's t-test was performed between experiment and simulation.

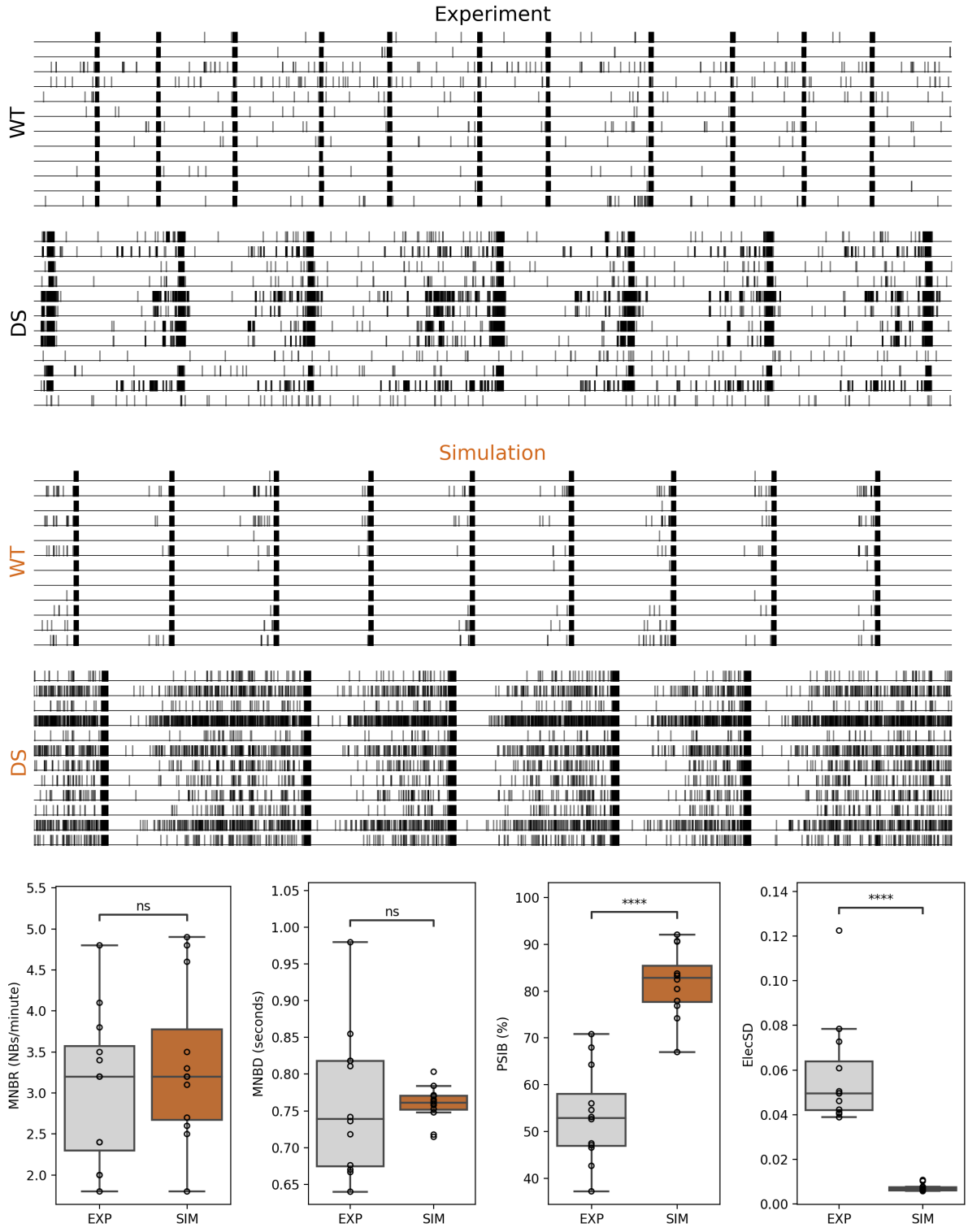

Figure 13: Comparison of DS behavior as observed from experiment (EXP) and simulations (SIM). Top: representative raster plots of 120 seconds from WT and DS of the experiment and simulations. Bottom: boxplots of the output measures of 12 wells and 12 simulations. ns $P>0.05$, **** $P<0.0001$, Welch's t-test was performed between experiment and simulation.

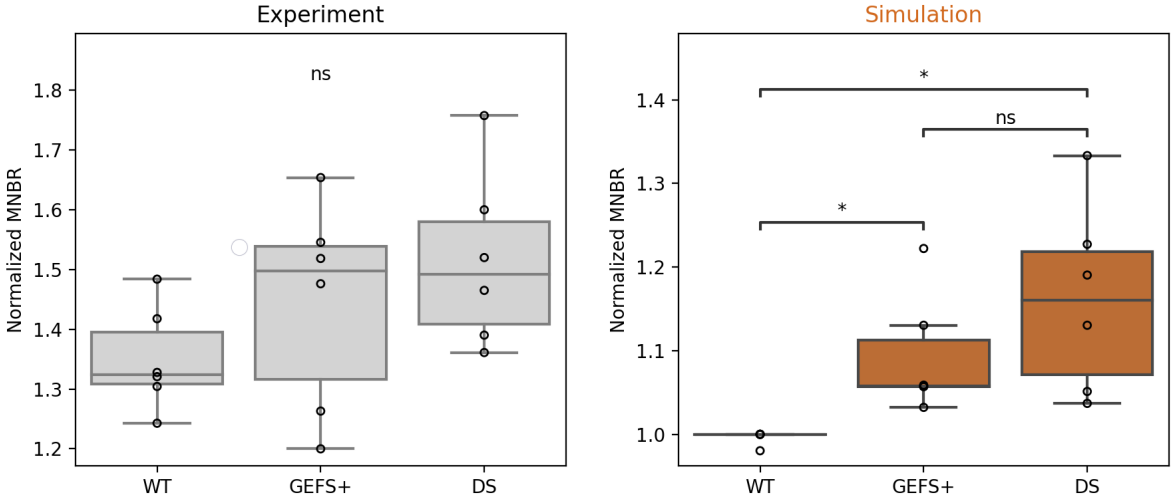

Figure 14: The effect of temperature on the MNBR of WT, GEFS+ and DS neuronal networks in experiment and simulations. Box plots of the normalized MNBR (40°C/37°C) of experiment and simulations are shown. Note that the y-scales are different. We see that the trend of the simulations appears to be the same as experimentally observed. However, while no significant differences are found between groups in experiments (one-way ANOVA $p>0.05$), there are slight significant differences in simulations. Moreover, experiments show larger relative increases in MNBR compared to simulations for all types. ns $P>0.05$, * $0.01<P<0.05$, one-way ANOVA with Welch correction and post-hoc Games-Howell.

4.2.6 GEFS+ and DS model validation

The results of the GEFS+ and DS model validation are shown in Figure 14. In experiments, we observed that increasing the temperature from 37°C to 40°C resulted in a significantly increased MNBR in WT, GEFS+, and DS networks. Unexpectedly, there are no significant differences in normalized MNBR (40°C/37°C) between the groups (WT, GEFS+, and DS) in the experiment (one-way ANOVA $p=0.11$). Simulations with the WT model show no increase in MNBR when the temperature is increased. However, there is a significant increase in MNBR in both GEFS+ and DS simulations. In contrast to experiment, there are slight significant differences between the groups in simulations (one-way ANOVA with Welch correction, $p=0.008$). Simulations with the GEFS+ model and the DS model both showed a slightly higher normalized MNBR than WT (post-hoc Games-Howell, $p=0.047$ and $p=0.035$ respectively).

5 | Discussion

5.1 WT model results

We used an *in silico* model comprising 100 HH-neurons to simulate the behavior of WT *in vitro* neuronal networks. Our model successfully simulated essential features of experimentally observed network behavior, like the MNBR and MNBD (see Figure 10). However, there were also some distinct differences between experiment and simulations.

PSIBs in simulations are significantly higher than those measured in experiments. The main cause appears to be that neurons in simulations spike with a higher frequency during an NB than neurons in experiment. This is because, in an NB, every neuron receives a large amount of synaptic current input caused by the high connectivity of the network [20]. In a burst, all neurons participate and reinforce the NB. We see that if we dramatically increase the number of neurons (for example to 10.000) and reduce the connectivity, the synaptic current every neuron receives in NBs lowers. This causes the neuron spike rate in NBs, and thereby the PSIB, to decrease. The high PSIB is thus likely a consequence of the small number of neurons in the model.

The ElecSD in the simulations is much lower than in experiments. This means that there are larger differences between the 12 electrode measurements *in vitro*. One reason is that, in our model, all neurons are homogeneously distributed over the area with the electrodes, whereas the electrodes in cultures may have many neurons close by or none at all. Additionally, other inhomogeneities, such as the nearby presence of the astrocytes, can impact the electrode recording [46]. Another reason for the large difference in ElecSD between experiment and simulation is that almost all neurons contribute to the NB in simulations, while this might not be the case in the cultures. Other studies with models of cultured neuronal networks also noted this difference between their simulations and experiments [15, 20, 21]. The reason all neurons participate could be the small number of neurons and the low amount of heterogeneity between the neurons in the model [21]. Even though some neurons are more active than others, they will all become active within an NB due to the high connectivity. PSIB and ElecSD can still be useful measures despite their significant differences between experiment and simulation because they capture the difference between healthy and GEFS+/DS behavior *in vitro*. We would like to see the same trend of lowered PSIB and heightened ElecSD in the GEFS+ and DS simulations, as we see in the experiments.

The output measures from our simulations show a more narrow distribution than the output measures of experimental recordings (see Figure 10). This most likely reflects biological differences between the wells in experiment; these differences are not included in the model. Mainly the amount and distribution of alive and functional neurons and astrocytes per well have been shown to affect neuronal network functionality [8]. Moreover, slight variations in routine cell culturing and maintenance, such as variation in the culture medium, can have significant effects on the network behavior [69]. This may cause differences in the output measures of experiments that can not be obtained with the different random number realizations in simulations.

We validated the WT model using the same experimental intervention *in vitro* and *in silico*. In experiments, the NMDA- and the AMPA-receptors of the cultured neurons were blocked. For simulations, we removed the NMDA and AMPA synaptic currents from the neurons. The resulting simulations reproduce the characteristics of the experimental observations (see Figure 11). The main consequence of the blocking of NMDA-receptors is shortening of the NB. In simulations, the amount of shortening is always the same, while the values for normalized MNBD in experiments vary more. This could again be caused by inhomogeneities not accounted for in the model. For example, every model neuron receives the same ratio of AMPA and NMDA current, while in cultures, the ratio of AMPA- and NMDA-receptors could differ per synapse [70]. Previous studies on rodent-derived neuronal networks and hiPSC derived neuronal networks showed that burst duration is directly influenced by AMPA and NMDA-receptors [52, 71]. Therefore, it is likely that, because the change in NMDA/AMPA ratio is equal for all simulations when blocking NMDA-receptors, the MNBD will also shorten equally for every simulation. Also

note that only four experimental measurements were available, and thus also only four simulations were used. Repeating this experiment might reveal other effects of the NMDA-receptor blocking. In the representative rasterplots of the experiment and simulation with AMPA-receptor blockage (see Figure 11), it appears that neurons in the simulation are more active than neurons in experiment. However, the difference in the amount of measured APs could also be due to the method of detecting the APs. The threshold for AP detection is based on the root mean square of the signal. The experimental signals generally are noisier, and thus their threshold for AP detection will be higher, especially when there are no NBs.

It could be argued that the used validation method is somewhat limited, as it only evaluates the AMPA and NMDA synaptic current implementation. However, we observed that most of the modeled mechanisms influence one another. For example, because NMDA blocking decreases NB duration, the level of spike-frequency adaptation and thereby NB rate are also altered. Other modeling studies have also reported such interplay between different modeled mechanisms [19–21]. Therefore, this validation method goes beyond the scope of synaptic currents. Nevertheless, more validation experiments could improve the validation, as will also be discussed in section 5.4.

Increasing the temperature in the WT model does not increase the MNBR like observed in experiments (see Figure 14). Temperature is only included in the model as a Q10 on the rates of change of the conductance gating variables. However, temperature dependencies of other processes are also suggested, like STD [72] and the amplitude of excitatory PSPs [73, 74]. Still, the effect of temperature on the network can be used to compare WT, GEFS+, and DS network behavior. However, conclusions should be drawn with caution since apparently, not all temperature mechanisms are properly included in the model.

5.2 GEFS+ and DS model results

We attempted to model the GEFS+ and DS neuronal networks by modifying the WT model. We included modification parameters in the HH equations to model changes in voltage-gated sodium channel dynamics. We found that changes in sodium channel dynamics by themselves could not reproduce the behavior of the GEFS+ and DS networks observed experimentally. We were able to reproduce the experimentally observed behavior by increasing the neuron excitability with the modification parameters and lowering the synaptic scaling factor S and the strength of the adaptive mechanisms (STD and spike-frequency adaptation).

The MNBR and MNBD of both GEFS+ and DS behavior could be replicated with the resulting models. In both GEFS+ and DS simulations, we also observe a lower PSIB compared to WT simulations. This agrees with the trend we see *in vitro*. However, PSIB is still higher than experimentally observed, which is presumably due to a higher firing rate in model neurons as discussed above. It can also be seen from the representative rasterplots in Figure 12 and 13, that there appears to be more activity outside the bursts in simulations than in experiments, even though the PSIB is higher in simulations.

For DS simulations, we observe an expected higher ElecSD compared to WT, while we did not see this in GEFS+ simulations. The NBs in DS are longer than those in GEFS+; this gives more room for variability between electrodes, explaining the increased ElecSD. However, in both GEFS+ and DS, the ElecSD is significantly lower than observed in experiments. A possible cause could be the small number of neurons with high connectivity. It appears in the experiments that some neurons contribute much less to the NB, while in simulations every neuron contributes approximately evenly. One can imagine that in the neuronal networks, when the synaptic strengths are downscaled, some groups of neurons might be partly disconnected from the rest of the network. This is supported by the hypothesis that cultured neuronal networks have highly connected subgroups of neurons, only lightly connected to other subgroups [75, 76]. With only 100 neurons, we can not observe these groups or the de-coupling of groups. We therefore attempted to model DS with 10.000 neurons and a more realistic topology. This is further explained in Appendix B. In simulations with these large networks, we still do not see the amount of change in ElecSD seen in experiments between WT and the pathologies. Another possible explanation is that there is more heterogeneity in the neuron population than we modeled. There are significant variances observed in the intrinsic properties of neurons derived from hiPSCs; for example,

the rheobase and maximum spike frequency can differ largely from one neuron to another [77]. This could cause some neurons to be more susceptible to the change in sodium channel dynamics than others. The neurons in the model are relatively homogeneous and have exactly the same modification of their sodium channel. More heterogeneities can be incorporated in the neuron equations to potentially affect the ElecSD.

In the GEFS+ and DS model validation, simulations appear to follow the same trend as experimental observations (see Figure 14). However, there are no significant differences between the normalized MNBR of the three groups in the experiment. We did expect to find a difference, as both GEFS+ and DS are clinically often responsive to temperature [4, 33, 35]. In simulations, there are slight differences in normalized MNBR between the groups. This disparity between experiment and simulations could arise from incomplete or incorrect modeling of temperature dependencies; after all, the normalized MNBRs of all groups are lower in simulations compared to experiment. However, the difference in significance may well be a result of the limited dataset available [78]. As GEFS+ and DS neurons are likely responsive to elevated temperature [79, 80], it is valuable to investigate this matter further.

5.2.1 Interpretation of modifications

Besides using the modification parameters, we altered S and the strength of the adaptive mechanisms to obtain the GEFS+ and DS models. Here we will try to interpret these parameter changes. We lowered the value of S, which is a variable that scales all the synaptic weights. This synaptic downscaling is something also observed *in vivo* [81] and *in vitro* [82]. Synaptic downscaling is a form of homeostatic plasticity, a group of mechanisms to promote stability in neuronal firing rates [83]. Homeostatic synaptic downscaling is a negative feedback response to persistently elevated network activity. Such downscaling is observed in *in vitro* networks when the neuronal network activity is artificially elevated [84]. The primary mechanism for synaptic downscaling is a decrease of AMPA-receptor numbers [82]. However, also the pre-synaptic neurotransmitter system can be altered [85]. When the activity of all neurons increases, all synaptic strengths of the excitatory synapses can decrease [83]. Previous research with hiPSC derived excitatory neuronal networks showed that homeostatic synaptic plasticity was present in these networks [52]. They found that insertion of AMPA-receptors was initiated by neuronal inactivity. Similarly, in our networks, AMPA-receptors numbers could be decreased as a response to the heightened network activity due to the sodium channel modifications. Thus, a decrease of S could correspond to homeostatic synaptic plasticity.

To counteract the burst shortening effect of the synaptic downscaling, we lowered the effect of STD and spike-frequency adaptation. A lowered STD could be caused by homeostatic synaptic plasticity. Deperrois et al. [86] showed that long-term synaptic depression can lower STD, for example by a reduction in neurotransmitter release. Since we use a phenomenological model for STD, we have to manually lower the strength of STD to account for this effect. The decreased spike-frequency adaptation can be interpreted as a result of the sodium channel mutations. In the model, we use one simple mechanism of spike-frequency adaptation to model the effect of all possible mechanisms. One mechanism for spike-frequency adaptation is the use-dependence of channel activity. Spampanato et al. [36] showed that two mutations resulting in GEFS+ caused a decrease in the use-dependence of channel activity. This could thus cause a decrease in spike-frequency adaptation. We can see from the representative raster plots in Figure 12 that in the experiments, the time after a burst when the neurons are somewhat silent, seems to disappear in the GEFS+ cultures. This also suggests that spike-frequency adaptation might be suppressed.

For both STD and spike-frequency adaptation, more biologically realistic mechanisms could be modeled. In that way, it could be tested if the mechanisms mentioned above and their interactions can explain the lengthening of the bursts. Costa et al. [87] proposed a model which accounts for the change in STD through long-term plasticity mechanisms. Benda et al. [88] proposed a phenomenological model for spike-frequency adaptation that encompasses all possible mechanisms. Currently, we did not include a homeostatic plasticity model, nor other forms of long-term synaptic plasticity. This is because these forms of plasticity would take time to show an effect. The simulations used in this research are computationally expensive, and the simulation times are approximately twice the simulated times. Therefore, simulation of long-term effects would take weeks. Moreover, this research does not focus on long-term changes in behavior but only looks at stationary behavior. To closely investigate the

interaction between all above-mentioned mechanisms, it might be helpful to use a simple, more efficient model, e.g. with LIF neurons, including homeostatic synaptic plasticity and other long-term effects. Toyoizumi et al. [89] propose a model to capture the interaction between homeostatic synaptic plasticity and other forms of long-term synaptic plasticity.

5.2.2 Multiple possible models

It is possible to simulate the GEFS+ and DS network behavior in multiple ways. Different choices of the modification parameters result in simulations with the same MNBR and MNBD as observed in the GEFS+ and DS cultures. Previous research with single neuron models of GEFS+ and DS also showed that different channel modifications resulted in the same change in neuron behavior [26, 28]. Figure 12 and 13 show one example of a combination of modifications that results in behavior similar to that observed *in vitro*. We can thus identify candidate mechanisms that cause hyperexcitability in neurons, but we cannot narrow it down to one mechanism. Using single neuron path-clamp measurement, more information could be obtained about the dynamics of the sodium channel [33, 36, 38]. This could narrow down the modeling possibilities. If the model then also incorporates biophysical STD, spike-frequency adaptation, and homeostasis models, it could potentially be used to identify and test AEDs [2, 90, 91]. The use of drugs could also be a way to validate the model [92]. The effect of drugs can be predicted using several models with different sodium channel dynamics. The model that best predicts the behavior of the cultures where the drug is administered, is then the most likely.

We decided to further analyze one model possibility for GEFS+ and one for DS. The GEFS+ patient from whom the neurons in the cultures originate has a mutation in the voltage-sensing domain of the sodium channel. Therefore, it seemed sensible to model a change in the voltage dependency of the sodium channels. We modeled a hyperpolarized shift in the voltage-dependence of activation and inactivation, which was also found in another GEFS+ mutant sodium channel [37]. One would think that the shift in inactivation would lead to decreased excitability of the neuron. However, since both activation and inactivation move in the same direction, the window current (the voltage region where the sodium channels can continue to open between activation and inactivation), will move to lower voltages where the membrane potential of the neuron more often resides. Therefore, the neuron is more often activated and thus hyperexcitable.

The patient with DS has a missense mutation in the pore domain of the sodium channel. Therefore, we chose to model a higher rate of activation of the m-gate. This accelerated activation was also found in other research, where it was caused by a mutation that resulted in a GEFS+ like clinical phenotype [93].

5.3 Implications

The question remains what the above-analyzed findings implicate for GEFS+ and DS. Earlier research with single neuron models showed some mutations associated with GEFS+ and DS resulted in neuron hyperexcitability [26, 28]. They argue that this neuron hyperexcitability could be the cause of epilepsy. With this research, we showed that if the model is correct, neuron hyperexcitability alone can not explain the network behavior of GEFS+ and DS neurons. Network modifications are needed to obtain the GEFS+ and DS behavior. The most important candidate mechanism we identified for this is homeostatic plasticity. We predict that the synaptic strengths in the GEFS+ and DS neuronal networks are significantly lower compared to WT networks. This prediction can be tested by measuring the amplitude of miniature excitatory PSPs (mEPSPs) in the cultures. If homeostatic plasticity indeed has a significant effect on these epileptic networks, this also gives rise to new hypotheses regarding some mechanisms of epilepsy. Something that remains largely unknown is why patients with the same genetic mutation, even within the same family, can show a severely different clinical phenotype, ranging from benign forms of GEFS+ to DS. Moreover, studies investigating correlations between SCN1A mutations and phenotype severity have not found a reliable correspondence [94–97]. The amount of homeostatic plasticity might vary per patient based on genetic background or other factors. Therefore, we identify the amount of homeostatic plasticity as a candidate mechanism for phenotype-variability.

Another partly unexplained characteristic of DS is the developmental delay in language, motor function, learning and social skill of patients. To our knowledge, no linkage between the type of SCN1A mutation and cognitive outcome has been found [98, 99], or between environmental factors and cognitive outcome [100]. This suggests another mechanism might influence cognitive outcome. Swann et al. [101] argue that homeostatic mechanisms are actively engaged in the epileptic brain. These mechanisms try to re-establish normal neuronal network activity. In some forms of intractable epilepsies, like DS, seizures are so intense and frequent that these mechanisms cannot restore normal activity levels. Nevertheless, homeostatic mechanisms remain active and could become maladaptive, meaning the mechanisms are driven to such extremes that they induce undesirable effects. Swann et al. argue, by analyzing multiple mechanisms of homeostasis, that this maladapiveness could result in learning impairment. High amounts of homeostatic plasticity could thus potentially be a mechanism that causes the learning impairments observed in children with DS.

To our knowledge, this model is a unique combination of a detailed neuron model in a network structure calibrated to human neuronal network activity. Other research used single neuron models [26–28], or network models with simple neuron models [15–25]. Research with detailed neuron models in a network context is often not calibrated to experiments [22], or is too complicated, meaning they have numerous neuronal types organized in complicated multi-layer structures [102]. Our model is simple in that it only includes one type of excitatory neurons and one type of connections. This makes our model easy to compare to excitatory neuron cultures. Our *in silico* model can faithfully replicate the behavior of the human *in vitro* neuronal networks with accurate time scales. Mechanisms underlying experimental observations can be investigated with this model, while model predictions can be confirmed in the cultures. Therefore, this model forms a useful tool to accompany research with hiPSC neuron cultures on genetic disorders.

5.4 Limitations

5.4.1 Number of neurons

We modeled only 100 neurons, while cultures consist of about 20.000 neurons. As more elaborately discussed in appendix B, increasing the number of neurons did not change the essential characteristics of the network behavior, such as the MNBD and MNBR. Other modeling studies found a similar effect of increasing the number of neurons [16, 19]. However, increasing the number of neurons did result in more realistic maximum spike rates in NBs and larger differences between electrode measurements. Because we look at relative changes in network behavior from WT to GEFS+ and DS, we do not think the number of neurons influences the conclusions.

5.4.2 One-compartment model

We modeled neurons using a one-compartment model with only one type of voltage-gated sodium channels. However, there are distinct differences between the dendrites, axon, and soma of neurons in voltage-gated channel expression [103]. Also, the $Na_v1.1$ expression is not homogeneous throughout the neuron [104]. These channels are predominantly expressed in the initial segments of axons. We modeled changes in $Na_v1.1$ dynamics as if all voltage-gated sodium channels, or a subset homogeneously distributed throughout the neuron, were altered. In reality, only a subset of channels in a specific part of the neuron might be altered. This could result in complex neuron dynamics that we did not find in our simulations. To map the extend of the effect of our simplification, it might be useful to research the difference in neuron dynamics between one-compartment models and multi-compartment models with heterogeneous $Na_v1.1$ channel distribution.

5.4.3 Parameter values

A lot of the parameter values used for the WT model were not based on experimental measurements. Examples are the degree of spike-frequency adaptation and STD, the timescale of spike-frequency adaptation, and the amount of noise every neuron receives. The used values are tweaked in such a way that the simulations resembled the experimentally observed behavior. However, it often became apparent that multiple combinations of parameters resulted in roughly the same behavior. For example, to increase the MNBR, one can increase the synaptic strength, increase the amount of noise every neuron

receives or shorten the time scale of spike-frequency adaptation. The certainty of these parameter values can be improved by performing more model validations. More experimental manipulations can be compared to model manipulations [105]. Moreover, more output measures can be taken into account, such as the distribution of the inter-NB-intervals [105]. For example, this distribution will be more narrow if the burst rate is more determined by strong synapses rather than a lot of noise.

6 | Conclusion and Recommendations

This research aimed to elucidate the role of sodium channel mutations and network dynamics in explaining *in vitro* observations of GEFS+ and DS neuronal networks using a biophysical computational model. We combined elements of existing models to obtain a detailed neuronal network model comprising 100 HH neurons. Our model faithfully reproduces the behavior of WT cultures. Modifications of the voltage-gated sodium channel were insufficient to transition to a GEFS+ or DS model. Additional downscaling of the synaptic weights and adaptive mechanisms resulted in simulations that did reproduce the experimentally observed behavior of GEFS+ and DS neuronal networks. We identify homeostatic plasticity as a candidate mechanism responsible for a large part of the GEFS+ and DS network dynamics.

To further verify our newly gained hypothesis, we have several recommendations for further research. First, a computational model could be made that includes biophysical models of long-term synaptic plasticities and their effects on short-term plasticity. In this way, we can test whether the interplay of these mechanisms is as we hypothesized here based on literature. Second, our predictions about the significant role of homeostatic plasticity in GEFS+ and DS networks can be partially confirmed by measuring mEPSPs in the neuron cultures. We predict that mEPSPs in GEFS+ and DS cultures will be significantly lower than in WT cultures.

This model forms a unique and valuable tool to accompany research with cultured neuronal networks derived from hiPSCs. By utilizing either more experimental measurements or performing more validations, the modeling possibilities for the GEFS+ and DS networks could be further narrowed down, and more precise models can be obtained. These models can then potentially be used to make more predictions about important mechanisms or the effectiveness of different AEDs. Moreover, the model could be calibrated to cultures of other genetic pathologies to assist in unraveling these disorders.

References

1. Ngugi, A. K., Bottomley, C., Kleinschmidt, I., Sander, J. W. & Newton, C. R. Estimation of the burden of active and life-time epilepsy: A meta-analytic approach. *Epilepsia* **51,** 883–890. ISSN: 00139580 (May 2010).
2. Helling, R. M., Petkov, G. H. & Kalitzin, S. N. *Expert system for pharmacological epilepsy treatment prognosis and optimal medication dose prescription* in *ACM International Conference Proceeding Series* (Association for Computing Machinery, Jan. 2019). ISBN: 9781450360852.
3. Scanlon, A. & Cook, S. S. Febrile seizures, genetic (Generalized) epilepsy with febrile seizures plus, and dravet's syndrome. *Journal for Specialists in Pediatric Nursing* **15,** 154–159. ISSN: 15390136 (Apr. 2010).
4. Scheffer, I. E., Zhang, Y. H., Jansen, F. E. & Dibbens, L. Dravet syndrome or genetic (generalized) epilepsy with febrile seizures plus? *Brain and Development* **31,** 394–400. ISSN: 03877604 (May 2009).
5. Guerrini, R. *et al.* Lamotrigine and seizure aggravation in severe myoclonic epilepsy. *Epilepsia* **39,** 508–512. ISSN: 00139580 (May 1998).
6. Lossin, C. A catalog of SCN1A variants. *Brain and Development* **31,** 114–130. ISSN: 03877604 (Feb. 2009).
7. Chen, S. J. & Hirose, S. Current proceedings of febrile seizures and related epileptic syndromes in SCN1A: From bedside to bench. *Journal of Medical Sciences* **29,** 167–172. ISSN: 10114564 (2009).
8. Mossink, B. *et al.* Human neuronal networks on micro-electrode arrays are a highly robust tool to study disease-specific genotype-phenotype correlations in vitro. *bioRxiv,* 2021.01.20.427439 (Jan. 2021).
9. Duch, W. Computational models of dementia and neurological problems. *Methods in molecular biology (Clifton, N.J.)* **401,** 305–336. ISSN: 10643745 (2007).
10. Prinz, A. A. Computational approaches to neuronal network analysis. *Philosophical Transactions of the Royal Society B: Biological Sciences* **365,** 2397–2405. ISSN: 14712970 (Aug. 2010).
11. Nowinski, W. L. Computational and mathematical methods in brain atlasing. *Neuroradiology Journal* **30,** 520–534. ISSN: 19714009 (Dec. 2017).
12. González, J. *et al.* Advances in Astrocyte Computational Models: From Metabolic Reconstructions to Multi-omic Approaches. *Frontiers in Neuroinformatics* **14.** ISSN: 16625196 (Aug. 2020).
13. Seo, H. & Jun, S. C. Multi-scale computational models for electrical brain stimulation. *Frontiers in Human Neuroscience* **11.** ISSN: 16625161 (2017).
14. Einevoll, G. T., Kayser, C., Logothetis, N. K. & Panzeri, S. Modelling and analysis of local field potentials for studying the function of cortical circuits. *Nature Reviews Neuroscience* **14,** 770–785. ISSN: 1471003X (2013).
15. Gritsun, T. A., Le Feber, J., Stegenga, J. & Rutten, W. L. Network bursts in cortical cultures are best simulated using pacemaker neurons and adaptive synapses. *Biological Cybernetics* **102,** 293–310. ISSN: 03401200 (Apr. 2010).
16. Gritsun, T., Le Feber, J., Stegenga, J. & Rutten, W. L. Experimental analysis and computational modeling of interburst intervals in spontaneous activity of cortical neuronal culture. *Biological Cybernetics* **105,** 197–210. ISSN: 03401200 (Oct. 2011).
17. Gritsun, T. A., Feber, J. & Rutten, W. L. C. Growth Dynamics Explain the Development of Spatiotemporal Burst Activity of Young Cultured Neuronal Networks in Detail. **7** (2012).
18. Andalibi, V., Aaltonen, T., Christophe, F. & Mikkonen, T. *SiMEA: A framework for simulating neurons on multi-electrode array* in *Proceedings of the Annual International Conference of the IEEE Engineering in Medicine and Biology Society, EMBS* **2016-Octob** (Institute of Electrical and Electronics Engineers Inc., Oct. 2016), 5965–5968. ISBN: 9781457702204.

19. Wiedemann, U. A. & Lüthi, A. Timing of Network Synchronization by Refractory Mechanisms. *Journal of Neurophysiology* **90,** 3902–3911. ISSN: 00223077 (Dec. 2003).

20. Park, I., Xu, D., Demarse, T. B. & Principe, J. C. Modeling of synchronized burst in dissociated cortical tissue: An exploration of parameter space. *IEEE International Conference on Neural Networks - Conference Proceedings,* 581–586. ISSN: 10987576 (2006).

21. Masquelier, T. & Deco, G. Network Bursting Dynamics in Excitatory Cortical Neuron Cultures Results from the Combination of Different Adaptive Mechanism. *PLoS ONE* **8,** e75824. ISSN: 19326203 (Oct. 2013).

22. Kowalski, J. M., Albert, G. L., Rhoades, B. K. & Gross, G. W. Neuronal networks with spontaneous, correlated bursting activity: Theory and simulations. *Neural Networks* **5,** 805–822. ISSN: 08936080 (1992).

23. Kumar, R., Huang, Y.-T., Chen, C.-C. & Tzeng, S.-F. Astrocytic regulation of synchronous bursting in cortical cultures: from local to global. *Cerebral Cortex Communications,* 870915 (Dec. 2019).

24. Tsodyks, M., Uziel, A. & Markram, H. Synchrony generation in recurrent networks with frequency-dependent synapses. *The Journal of neuroscience : the official journal of the Society for Neuroscience* **20.** ISSN: 15292401 (2000).

25. Pasquale, V., Massobrio, P., Bologna, L. L., Chiappalone, M. & Martinoia, S. Self-organization and neuronal avalanches in networks of dissociated cortical neurons. *Neuroscience* **153,** 1354–1369. ISSN: 03064522 (June 2008).

26. Spampanato, J., Aradi, I., Soltesz, I. & Goldin, A. L. Increased Neuronal Firing in Computer Simulations of Sodium Channel Mutations That Cause Generalized Epilepsy with Febrile Seizures Plus. *Journal of Neurophysiology* **91,** 2040–2050. ISSN: 00223077 (2004).

27. Kahlig, K. M., Misra, S. N. & George, A. L. Impaired inactivation gate stabilization predicts increased persistent current for an epilepsy-associated SCN1A mutation. *Journal of Neuroscience* **26,** 10958–10966. ISSN: 02706474 (Oct. 2006).

28. Berecki, G. *et al.* SCN1A gain of function in early infantile encephalopathy. *Annals of Neurology* **85,** 514–525. ISSN: 15318249 (Apr. 2019).

29. Izhikevich, E. M. Simple model of spiking neurons. *IEEE Transactions on Neural Networks* **14,** 1569–1572. ISSN: 10459227 (Nov. 2003).

30. Fisher, R. S. *et al.* ILAE Official Report: A practical clinical definition of epilepsy. *Epilepsia* **55,** 475–482. ISSN: 15281167 (2014).

31. Tidball, A. M. & Parent, J. M. Concise Review: Exciting Cells: Modeling Genetic Epilepsies with Patient-Derived Induced Pluripotent Stem Cells. *STEM CELLS* **34,** 27–33. ISSN: 10665099 (Jan. 2016).

32. Holmes, G. L. & Noebels, J. L. The epilepsy spectrum: Targeting future research challenges. *Cold Spring Harbor Perspectives in Medicine* **6.** ISSN: 21571422 (July 2016).

33. Lossin, C. *et al.* Epilepsy-Associated Dysfunction in the Voltage-Gated Neuronal Sodium Channel SCN1A. *Journal of Neuroscience* **23,** 11289–11295. ISSN: 02706474 (Dec. 2003).

34. Dravet, C., Bureau, M., Bernardina, B. D. & Guerrini, R. Severe myoclonic epilepsy in infancy (Dravet syndrome) 30 years later. *Epilepsia* **52,** 1–2. ISSN: 00139580 (Apr. 2011).

35. Singh, R. *et al.* Severe myoclonic epilepsy of infancy: Extended spectrum of GEFS+? *Epilepsia* **42,** 837–844. ISSN: 00139580 (2001).

36. Spampanato, J., Escayg, A., Meisler, M. H. & Goldin, A. L. Functional effects of two voltage-gated sodium channel mutations that cause generalized epilepsy with febrile seizures plus type 2. *Journal of Neuroscience* **21,** 7481–7490. ISSN: 02706474 (Oct. 2001).

37. Spampanato, J., Escayg, A., Meisler, M. H. & Goldin, A. L. Generalized epilepsy with febrile seizures plus type 2 mutation W1204R alters voltage-dependent gating of Nav1.1 sodium channels. *Neuroscience* **116,** 37–48. ISSN: 03064522 (Jan. 2003).

38. Lossin, C., Wang, D. W., Rhodes, T. H., Vanoye, C. G. & George, A. L. Molecular basis of an inherited epilepsy. *Neuron* **34,** 877–884. ISSN: 08966273 (2002).

39. Volkers, L. *et al.* Na v1.1 dysfunction in genetic epilepsy with febrile seizures-plus or Dravet syndrome. *European Journal of Neuroscience* **34,** 1268–1275. ISSN: 0953816X (2011).

40. Marini, C. *et al.* The genetics of Dravet syndrome. *Epilepsia* **52,** 24–29. ISSN: 00139580 (Apr. 2011).

41. Catterall, W. A. Dravet syndrome: a sodium channel interneuronopathy. *Current Opinion in Physiology* **2,** 42–50. ISSN: 24688673 (Apr. 2018).

42. Yu, F. H. *et al.* Reduced sodium current in GABAergic interneurons in a mouse model of severe myoclonic epilepsy in infancy. *Nature Neuroscience* **9,** 1142–1149. ISSN: 10976256 (Sept. 2006).

43. Liu, Y. *et al.* Dravet syndrome patient-derived neurons suggest a novel epilepsy mechanism. *Annals of Neurology* **74,** 128–139. ISSN: 03645134 (July 2013).

44. Jiao, J. *et al.* Modeling Dravet syndrome using induced pluripotent stem cells (iPSCs) and directly converted neurons. *Human Molecular Genetics* **22,** 4241–4252. ISSN: 09646906 (Nov. 2013).

45. Novellino, A. *et al.* Development of micro-electrode array based tests for neurotoxicity: Assessment of interlaboratory reproducibility with neuroactive chemicals. *Frontiers in Neuroengineering* **4,** 1–14. ISSN: 16626443 (Apr. 2011).

46. Obien, M. E. J., Deligkaris, K., Bullmann, T., Bakkum, D. J. & Frey, U. Revealing neuronal function through microelectrode array recordings. *Frontiers in Neuroscience* **9,** 423. ISSN: 1662453X (2015).

47. Takahashi, K. & Yamanaka, S. Induction of Pluripotent Stem Cells from Mouse Embryonic and Adult Fibroblast Cultures by Defined Factors. *Cell* **126,** 663–676. ISSN: 00928674 (Aug. 2006).

48. Shi, Y., Inoue, H., Wu, J. C. & Yamanaka, S. *Induced pluripotent stem cell technology: A decade of progress* Feb. 2017.

49. Soliman, M. A., Aboharb, F., Zeltner, N. & Studer, L. *Pluripotent stem cells in neuropsychiatric disorders* Sept. 2017.

50. Mertens, J., Marchetto, M. C., Bardy, C. & Gage, F. H. Evaluating cell reprogramming, differentiation and conversion technologies in neuroscience. *Nature Reviews Neuroscience* **17,** 424–437. ISSN: 14710048 (July 2016).

51. Sterlini, B. *et al.* Progress of induced pluripotent stem cell technologies to understand genetic epilepsy. *International Journal of Molecular Sciences* **21.** ISSN: 14220067 (2020).

52. Frega, M. *et al.* Neuronal network dysfunction in a model for Kleefstra syndrome mediated by enhanced NMDAR signaling. *Nature Communications* **10,** 4928. ISSN: 2041-1723 (2019).

53. Quraishi, I. H. *et al.* An epilepsy-associated KCNT1 mutation enhances excitability of human iPSC-derived neurons by increasing slack KNa currents. *Journal of Neuroscience* **39,** 7438–7449. ISSN: 15292401 (Sept. 2019).

54. Brodland, G. W. How computational models can help unlock biological systems. *Seminars in Cell and Developmental Biology* **47-48,** 62–73. ISSN: 10963634 (Dec. 2015).

55. Napoli, A. & Obeid, I. Comparative Analysis of Human and Rodent Brain Primary Neuronal Culture Spontaneous Activity Using Micro-Electrode Array Technology. *Journal of Cellular Biochemistry* **117,** 559–565. ISSN: 10974644 (Mar. 2016).

56. Hodgkin, A. L. & Huxley, A. F. A quantitative description of membrane current and its application to conduction and excitation in nerve. *The Journal of Physiology* **117,** 500–544. ISSN: 14697793 (Aug. 1952).

57. Van Vreeswijk, C. & Hansel, D. Patterns of synchrony in neural networks with spike adaptation. *Neural Computation* **13,** 959–992. ISSN: 08997667 (2001).

58. Latham, P. E., Richmond, B. J., Nelson, P. G. & Nirenberg, S. Intrinsic Dynamics in Neuronal Networks. I. Theory. *Journal of Neurophysiology* **83,** 808–827. ISSN: 0022-3077 (Feb. 2000).

59. Gutkin, B. & Zeldenrust, F. Spike Frequency Adaptation. *Scholarpedia* **9,** 30643 (2014).

60. Purves, D. *Neuroscience* ISBN: 9780878937424 (Palgrave Macmillan, 2001).

61. Markram, H., Wang, Y. & Tsodyks, M. Differential signaling via the same axon of neocortical pyramidal neurons. *Proceedings of the National Academy of Sciences of the United States of America* **95,** 5323–5328. ISSN: 00278424 (Apr. 1998).

62. Traub, R. D. & Miles, R. *Neuronal Networks of the Hippocampus* ISBN: 9780521364812 (Cambridge University Press, May 1991).

63. Thivierge, J. P. & Cisek, P. Nonperiodic synchronization in heterogeneous networks of spiking neurons. *Journal of Neuroscience* **28,** 7968–7978. ISSN: 02706474 (Aug. 2008).

64. Buzatu, S. The temperature-induced changes in membrane potential. eng. *Rivista di biologia* **102,** 199–217. ISSN: 0035-6050 (Print) (2009).

65. Roth, A. & van Rossum, M. C. W. in *Computational Modeling Methods for Neuroscientists* 139–160 (The MIT Press, Oct. 2013).

66. Jahr, C. E. & Stevens, C. F. Voltage dependence of NMDA-activated macroscopic conductances predicted by single-channel kinetics. *Journal of Neuroscience* **10,** 3178–3182. ISSN: 02706474 (Sept. 1990).

67. Müller, T. H., Swandulla, D. & Zeilhofer, H. U. Synaptic connectivity in cultured hypothalamic neuronal networks. *Journal of Neurophysiology* **77,** 3218–3225. ISSN: 00223077 (1997).

68. Stimberg, M., Brette, R. & Goodman, D. F. Brian 2, an intuitive and efficient neural simulator. *eLife* **8.** ISSN: 2050084X (Aug. 2019).

69. Volpato, V. & Webber, C. *Addressing variability in iPSC-derived models of human disease: Guidelines to promote reproducibility* Jan. 2020.

70. Strube, C., Gackière, F., Saliba, L., Tell, F. & Kessler, J.-P. Variability of quantal NMDA to AMPA current ratio in nucleus tractus solitarii neurons. *bioRxiv,* 110569 (Feb. 2017).

71. Suresh, J. *et al.* Network burst activity in hippocampal neuronal cultures: The role of synaptic and intrinsic currents. *Journal of Neurophysiology* **115,** 3073–3089. ISSN: 15221598 (2016).

72. Van Hook, M. J. Temperature effects on synaptic transmission and neuronal function in the visual thalamus. *PLoS ONE* **15,** e0232451. ISSN: 19326203 (Apr. 2020).

73. Schiff, S. J. & Somjen, G. G. The effects of temperature on synaptic transmission in hippocampal tissue slices. *Brain Research* **345,** 279–284. ISSN: 00068993 (Oct. 1985).

74. Zhu, Y., De Castro, L. & Cooper, R. L. Effect of temperature change on synaptic transmission at crayfish neuromuscular junctions. *Biology Open* **7.** ISSN: 20466390 (Dec. 2018).

75. Kwok, H. F., Jurica, P., Raffone, A. & Van Leeuwen, C. Robust emergence of small-world structure in networks of spiking neurons. *Cognitive Neurodynamics* **1,** 39–51. ISSN: 18714080 (2007).

76. Gafarov, F. M. Emergence of the small-world architecture in neural networks by activity dependent growth. *Physica A: Statistical Mechanics and its Applications* **461,** 409–418. ISSN: 03784371 (Nov. 2016).

77. Mossink, B. *et al.* Cadherin-13 is a critical regulator of GABAergic modulation in human stem cell derived neuronal networks. *bioRxiv,* 2020.05.07.082453 (May 2020).

78. Anscombe, F. J. The Validity of Comparative Experiments. *Journal of the Royal Statistical Society. Series A (General)* **111,** 181. ISSN: 00359238 (1948).

79. Peters, C., Rosch, R. E., Hughes, E. & Ruben, P. C. Temperature-dependent changes in neuronal dynamics in a patient with an SCN1A mutation and hyperthermia induced seizures. *Scientific Reports* **6.** ISSN: 20452322 (Sept. 2016).

80. Warner, T. A., Liu, Z., Macdonald, R. L. & Kang, J. Q. Heat induced temperature dysregulation and seizures in Dravet Syndrome/GEFS+ Gabrg2+/Q390X mice. *Epilepsy Research* **134,** 1–8. ISSN: 18726844 (Aug. 2017).

81. Lee, H. K. & Kirkwood, A. Mechanisms of Homeostatic Synaptic Plasticity in vivo. *Frontiers in Cellular Neuroscience* **13,** 520. ISSN: 16625102 (Dec. 2019).

82. O'Brien, R. J. *et al.* Activity-dependent modulation of synaptic AMPA receptor accumulation. *Neuron* **21,** 1067–1078. ISSN: 08966273 (1998).

83. Turrigiano, G. G., Leslie, K. R., Desai, N. S., Rutherford, L. C. & Nelson, S. B. Activity-dependent scaling of quantal amplitude in neocortical neurons. *Nature* **391,** 892–896. ISSN: 00280836 (Feb. 1998).

84. Siddoway, B., Hou, H. & Xia, H. Molecular mechanisms of homeostatic synaptic downscaling. *Neuropharmacology* **78,** 38–44. ISSN: 18737064 (Mar. 2014).

85. Erickson, J. D., De Gois, S., Varoqui, H., Schafer, M. K. & Weihe, E. Activity-dependent regulation of vesicular glutamate and GABA transporters: A means to scale quantal size. *Neurochemistry International* **48,** 643–649. ISSN: 01970186 (May 2006).

86. Deperrois, N. & Graupner, M. Short-term depression and long-term plasticity together tune sensitive range of synaptic plasticity. *PLOS Computational Biology* **16** (ed Cuntz, H.) e1008265. ISSN: 1553-7358 (Sept. 2020).

87. Costa, R. P., Froemke, R. C., Sjöström, P. J. & van Rossum, M. C. Unified pre- and postsynaptic long-term plasticity enables reliable and flexible learning. *eLife* **4.** ISSN: 2050084X (Aug. 2015).

88. Benda, J. & Herz, A. V. A Universal Model for Spike-Frequency Adaptation. *Neural Computation* **15,** 2523–2564. ISSN: 08997667 (Nov. 2003).

89. Toyoizumi, T., Kaneko, M., Stryker, M. P. & Miller, K. D. Modeling the Dynamic Interaction of Hebbian and Homeostatic Plasticity. *Neuron* **84,** 497–510. ISSN: 10974199 (Oct. 2014).

90. Weaver, D. F. in *Computational Neuroscience in Epilepsy* 515–529 (Elsevier Inc., 2008). ISBN: 9780123736499.

91. Kurbatova, P. *et al.* Dynamic changes of depolarizing GABA in a computational model of epileptogenic brain: Insight for Dravet syndrome. *Experimental Neurology* **283,** 57–72. ISSN: 10902430 (2016).

92. Wendling, F. Computational models of epileptic activity: A bridge between observation and pathophysiological interpretation. *Expert Review of Neurotherapeutics* **8,** 889–896. ISSN: 17448360 (2008).

93. Alekov, A. K., Masmudur Rahman, M. D., Mitrovic, N., Lehmann-Horn, F. & Lerche, H. Enhanced inactivation and acceleration of activation of the sodium channel associated with epilepsy in man. *European Journal of Neuroscience* **13,** 2171–2176. ISSN: 0953816X (2001).

94. Ohmori, I., Ouchida, M., Ohtsuka, Y., Oka, E. & Shimizu, K. Significant correlation of the SCN1A mutations and severe myoclonic epilepsy in infancy. *Biochemical and Biophysical Research Communications* **295,** 17–23. ISSN: 0006291X (July 2002).

95. Wallace, R. H. *et al.* Sodium channel α1-subunit mutations in severe myoclonic epilepsy of infancy and infantile spasms. *Neurology* **61,** 765–769. ISSN: 00283878 (Sept. 2003).

96. Fukuma, G. *et al.* Mutations of Neuronal Voltage-gated Na+ Channel α1 Subunit Gene SCN1A in Core Severe Myoclonic Epilepsy in Infancy (SMEI) and in Borderline SMEI (SMEB). *Epilepsia* **45,** 140–148. ISSN: 00139580 (Feb. 2004).

97. Delgado-Escueta, A. V. *Myoclonic Epilepsies Advances in neurology* **v. 95,** 103–117. ISBN: 9780781752480 (Lippincott Williams & Wilkins, 2005).

98. Ragona, F. Cognitive development in children with Dravet syndrome. *Epilepsia* **52,** 39–43. ISSN: 00139580 (Apr. 2011).

99. Ragona, F. *et al.* Cognitive development in Dravet syndrome: A retrospective, multicenter study of 26 patients. *Epilepsia* **52,** 386–392. ISSN: 00139580 (Feb. 2011).

100. Jansson, J. S., Hallböök, T. & Reilly, C. Intellectual functioning and behavior in Dravet syndrome: A systematic review. *Epilepsy and Behavior* **108,** 107079. ISSN: 15255069 (July 2020).

101. Swann, J. W. & Rho, J. M. How is homeostatic plasticity important in epilepsy? *Advances in Experimental Medicine and Biology* **813,** 123–131. ISSN: 22148019 (2014).

102. Van Drongelen, W. *et al.* Role of persistent sodium current in bursting activity of mouse neocortical networks in vitro. *Journal of Neurophysiology* **96,** 2564–2577. ISSN: 00223077 (2006).

103. Duménieu, M., Oulé, M., Kreutz, M. R. & Lopez-Rojas, J. The segregated expression of voltage-gated potassium and sodium channels in neuronal membranes: Functional implications and regulatory mechanisms. *Frontiers in Cellular Neuroscience* **11,** 115. ISSN: 16625102 (Apr. 2017).

104. Duflocq, A., Le Bras, B., Bullier, E., Couraud, F. & Davenne, M. Nav1.1 is predominantly expressed in nodes of Ranvier and axon initial segments. *Molecular and Cellular Neuroscience* **39,** 180–192. ISSN: 10447431 (Oct. 2008).

105. Staley, K., Swiercz, W. & Cios, K. J. in *Computational Neuroscience in Epilepsy* 43–47 (Elsevier Inc., 2008). ISBN: 9780123736499.

106. Baltz, T., Herzog, A. & Voigt, T. Slow oscillating population activity in developing cortical networks: models and experimental results. *Journal of Neurophysiology* **106,** 1500–1514. ISSN: 0022-3077 (Sept. 2011).

107. Watts, D. J. & Strogatz, S. H. Collective dynamics of 'small-world9 networks. *Nature* **393,** 440–442. ISSN: 00280836 (June 1998).

A | Bifurcation diagram

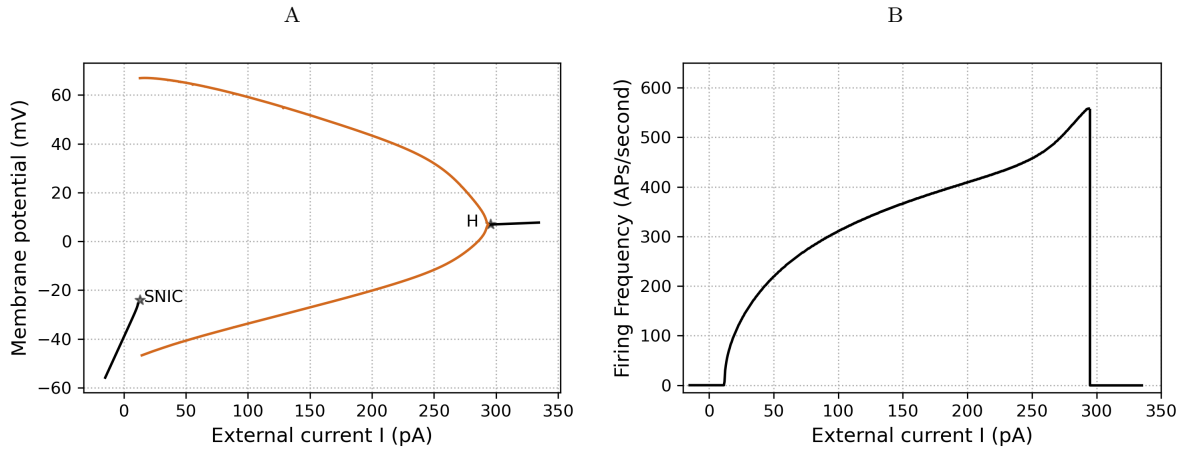

Figure A.1: Dynamics of the neuron model without spike-frequency adaptation. **A**. Simplified bifurcation diagram only showing stable equilibria. The black lines denote a stable fixed point. The orange lines denote the maximum and minimum values of V_m at the stable limit cycle. At the SNIC (Saddle-Node on an Invariant Circle) bifurcation, an undrawn saddle point collides with the stable fixed point and both disappear. Because these fixed points were on an invariant circle, their collision gives rise to a stable limit cycle. At H, a supercritical Hopf bifurcation (Lyapunov coefficient = -4.24e-3) occurs leading to a depolarization block. The stable limit cycle collides with an undrawn unstable fixed point, that then becomes a stable fixed point. **B**. I-F curve of the neuron model. The neuron starts firing when I exceeds the threshold I_{th}=12 pA. The neuron stops firing when the depolarization block is reached at I=292 pA

B | Number of neurons and connectivity

This appendix will elaborate on the effect of different numbers of neurons and different topologies on single neuron and network behavior. We will also attempt to simulate DS behavior with 10.000 neurons and small-world topology to see if this will result in more prominent differences between the measurements from the 12 electrodes.

B.1 Methods

B.1.1 Number of neurons

The number of neurons, N, can be set to any perfect square, such that the grid on which the neurons are placed is n times n, where $n = \sqrt{N}$. The remainder of the methods described in chapter 3 can be used, as these correct for the number of neurons (e.g., the conduction delay). We investigate the effect of the number of neurons using N=9, 16, 49, 100, 900, and 10.000. As we increase the number of neurons, we decrease either the connection probability or the synaptic scaling factor S. For the analysis, we look at the filtered electrode signals, rather than raster plots since the number of neurons mainly influences the shape of the NBs and since all electrodes pick up spikes from all neurons for small N.

B.1.2 Topologies

Different types of connectivity and topology have been used to model cultured neuronal networks. Masquelier et al. [21] used a full connectivity, which resulted in realistic network bursting behavior. Baltz et al. [106] used a random sparse connectivity with connection probabilities between 5- and 25%. A distant dependent connectivity was employed by Park et al. [20] and Pasquale et al. [25], with which they could replicate complicated network behavior. A small-world topology was proposed to be the origin of optimal network behavior in cultured neuronal networks by several researchers [17, 75, 76]. We investigated the effect of all these topologies on our neuronal network behavior. We will shortly discuss the implementation of these connectivities.

Random sparse connectivity
Neurons are randomly connected to other neurons with a connection probability P. P is set to 1 for a full connectivity and P<1 for a sparse connectivity. We investigate the effect of the connection probability for values P = 0.05, 0.1, 0.5, and 1.

Distance-dependent connectivity
Distant dependent connectivity was easily incorporated using the grid already in place. The probability that neurons i and j are connected depends on the euclidean distance, $d(i, j)$, between the neurons:

$$P(i, j) = \alpha e^{-\frac{d(i,j)}{2}}, \tag{36}$$

where α determines the chance of overall connectivity.

Small-world topology
A small-world network is a graph in which most nodes can be reached within a small number of steps (short average path length) and where nodes often appear in small, highly connected groups (high clustering). Because of this short path length, this graph is often proposed to be optimal for distributed information processing [75]. They are therefore often hypothesized to exist in neuronal networks [17, 75, 76]. To generate a small-world topology, we use a Watts-Strogatz model [107]. In short, a ring lattice is created of N nodes, where every node is connected to its K nearest neighbors. Then, for every node, every edge is rewired with probability p to a random other node, where self-loops are avoided. Thus, if p=0, there is a ring lattice structure, while if p=1, there is a random connectivity. In between, a

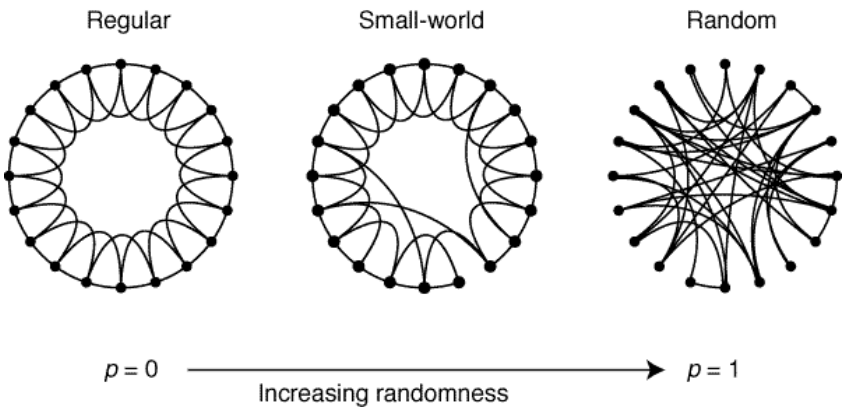

Figure B.1: Random rewiring procedure of the Watts-Strogatz model to obtain a small-world network. Image taken from [107].

small-world network appears. This is illustrated in Figure B.1. In the simulations, we use p=0.5. We take K to be N times the connection probability.

B.2 Results and discussion

B.2.1 Number of neurons

We already observe NB-like behavior in networks with 9 and 16 neurons, but we cannot obtain the correct time scales. NBs are much shorter, and the NB rate is much higher. With 49 neurons, accurate time scales can be obtained. From N=49 and up, the inter-NB-intervals and the NB durations become more narrowly distributed with a higher number of neurons. This is as expected since as there are more neurons, the noise will be more evened out. If we increase the number of neurons but do not decrease the connection probability, the NB durations will increase. If we increase the number of neurons but decrease the connection probability, the behavior of the network will stay qualitatively the same up to 10.000 neurons. The electrode measurements of an experiment and simulations with N = 49, 100, and 900 are shown in Figure B.2. The peak synaptic current does change as the number of neurons changes. For a low number of neurons, the connectivity (P or S) must be high to obtain the desired network behavior. This results in high peak synaptic currents at the start of NBs (around 250 pA). As a result, the firing frequency of the neurons is high and the amplitude of the APs is low, as can be foreseen from the I-F-curve and the bifurcation diagram in Figure 5. If we increase the number of neurons, the connectivity can be downscaled, and the peak synaptic current will lower (to approximately 180 pA). The shape of the burst will look more like observed in experiments. Examples of the membrane potential of a single neuron in an NB and of simulations with different numbers of neurons are shown in Figure B.3. Examples of the electrode measurements in an NB from an experiment and simulations with different numbers of neurons are shown in Figure B.4.

B.2.2 Topologies

For small numbers of neurons (N = 49, 100, 900), there is no observable difference in network behavior between a random sparse connectivity, a distant dependent connectivity, and a small-world topology. All these topologies are approximately random for small networks. Low connection probabilities result in too short NBs, while large values of P or a full connectivity can be compensated by lowering the value of S. For the large network of 10.000 neurons, the choice of topology introduces minor differences. Both the distance dependent connectivity and the small-world topology result in a network where the NBs are always initiated in the same small part of the network and then spread throughout the remainder of the network. This better replicates experimentally observed behavior. Examples of the electrodes measurements in an NB in experiment and a simulation with random connectivity, a simulation with distance-dependent connectivity, and a simulation with small-world topology are shown in Figure B.5

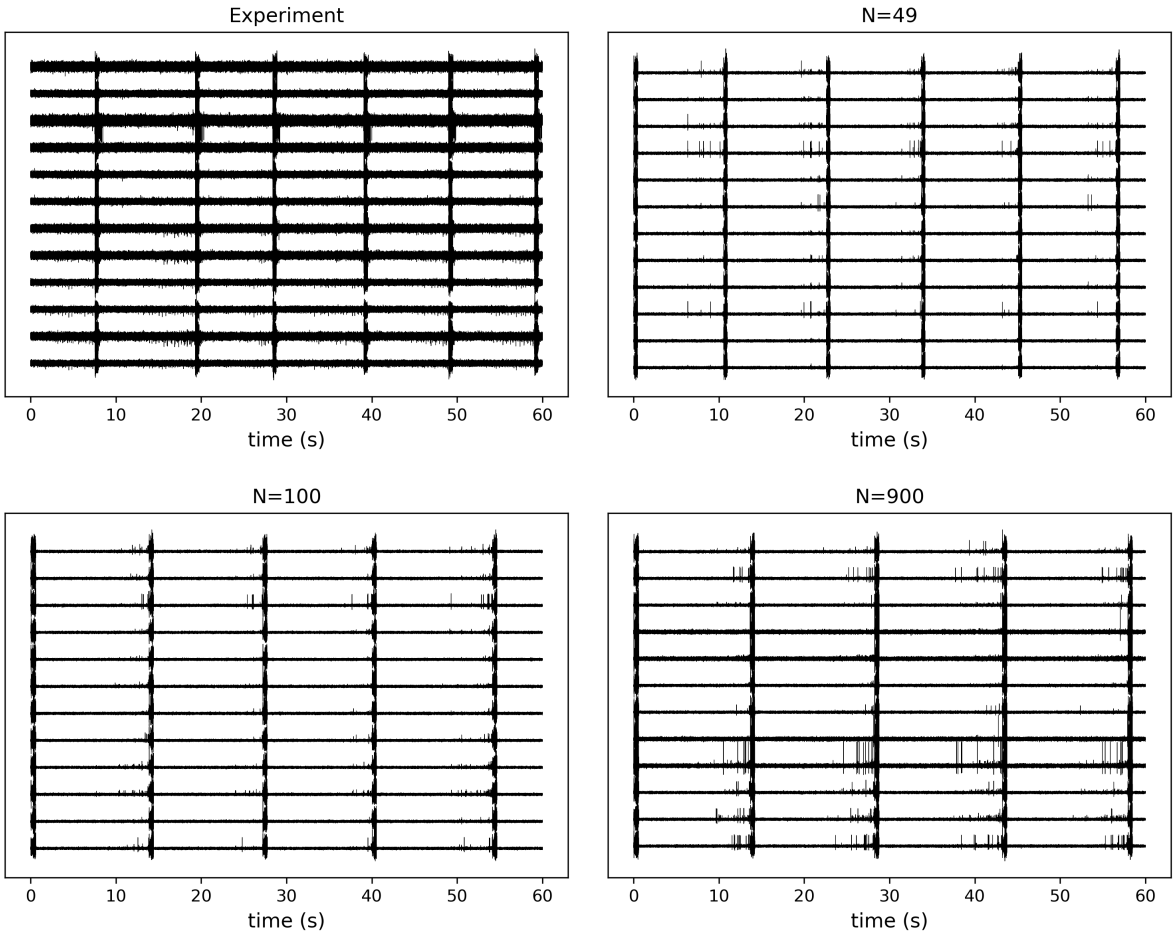

Figure B.2: Voltage recordings from 12 electrodes of one well from experiment, and from simulations with N=49, 100 and 900 neurons. The network behavior remains qualitatively the same for different numbers of neurons.

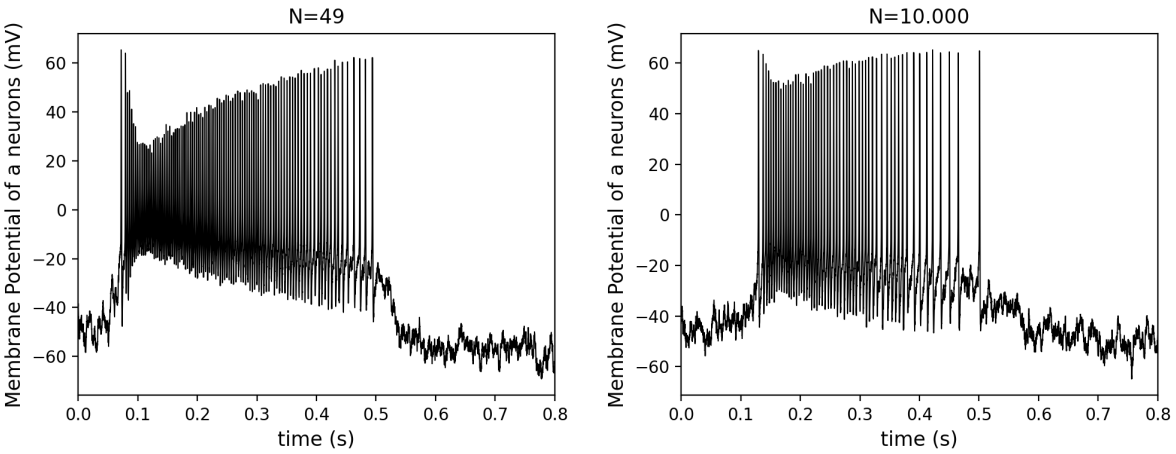

Figure B.3: Membrane potential of single neurons in a NB in a network with 49 and 10.000 neurons. We can see that for small networks at the start of an NB, the firing frequency of a single neuron is higher, and the AP amplitude is lower, compared to large networks. This is likely caused by a higher peak synaptic current.

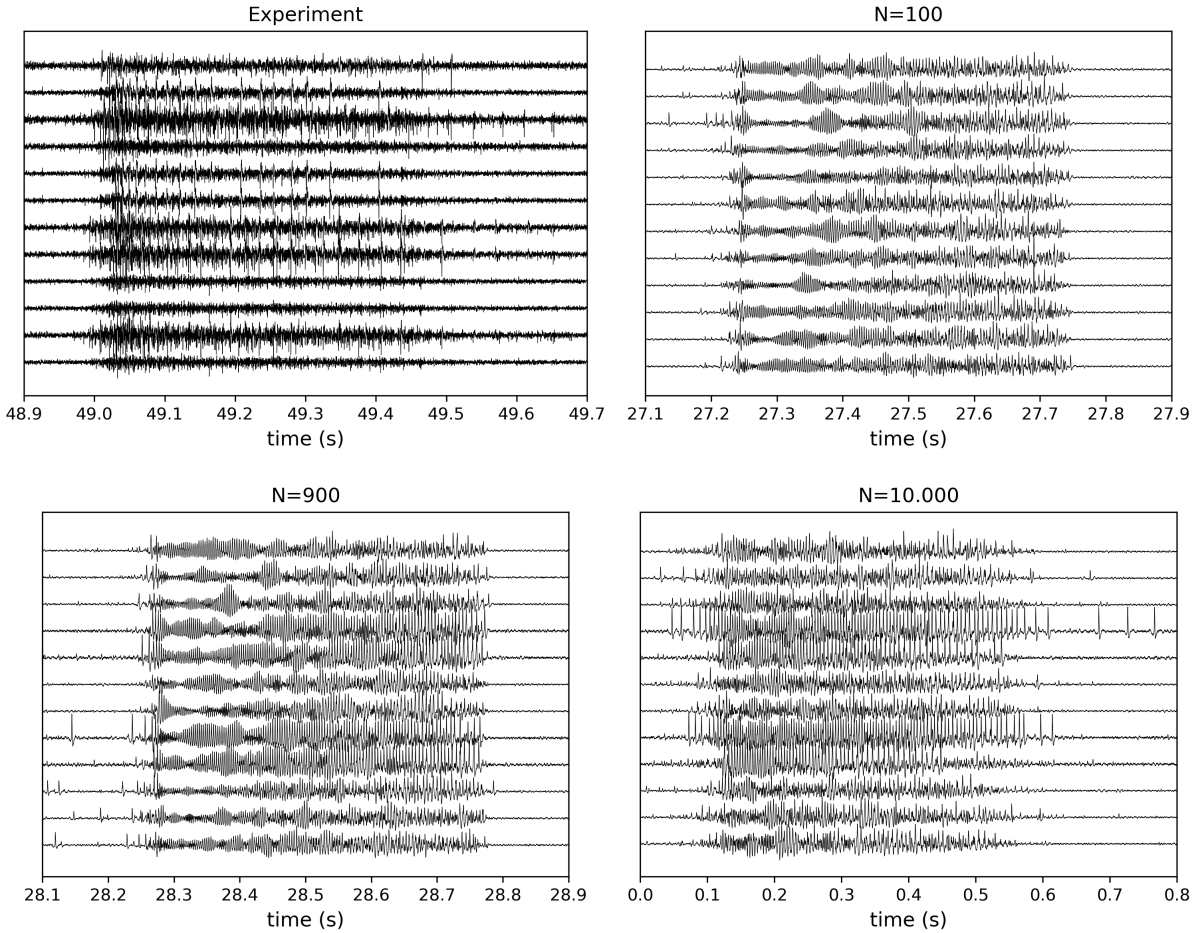

Figure B.4: Voltage recordings during a NB from 12 electrodes of one well from experiment, and from simulations with N=100, 900 and 10.000 neurons. Because of the low AP amplitudes of the neurons in small networks, the electrode signals look different from experimental observations at the start of an NB. In larger networks, the NBs look more like experiment.

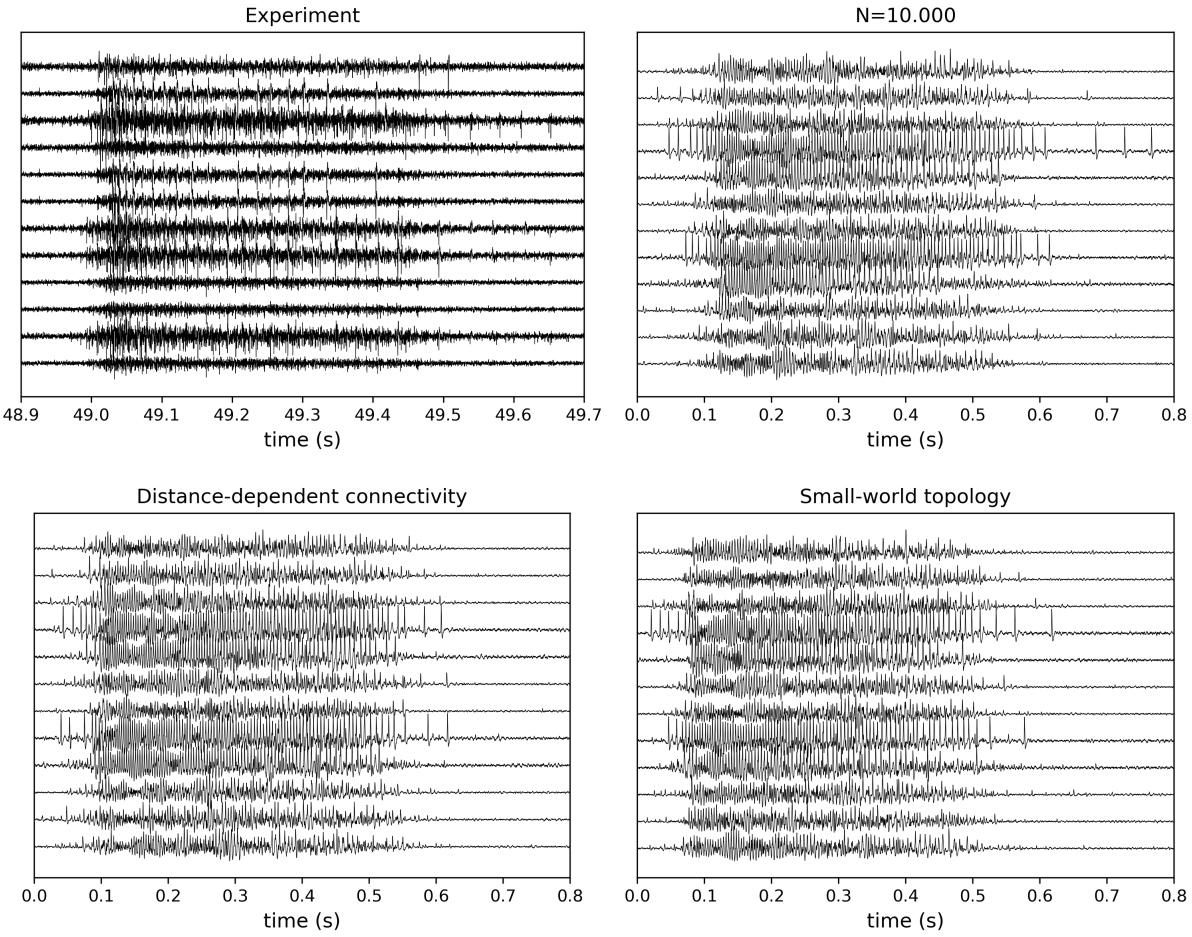

Figure B.5: Voltage recordings within a NB from 12 electrodes of one well from experiment, and from simulations with 10.000 neurons and different topologies, namely sparse connectivity (labelled N=10.000), distance-dependent connectivity and small-world topology.

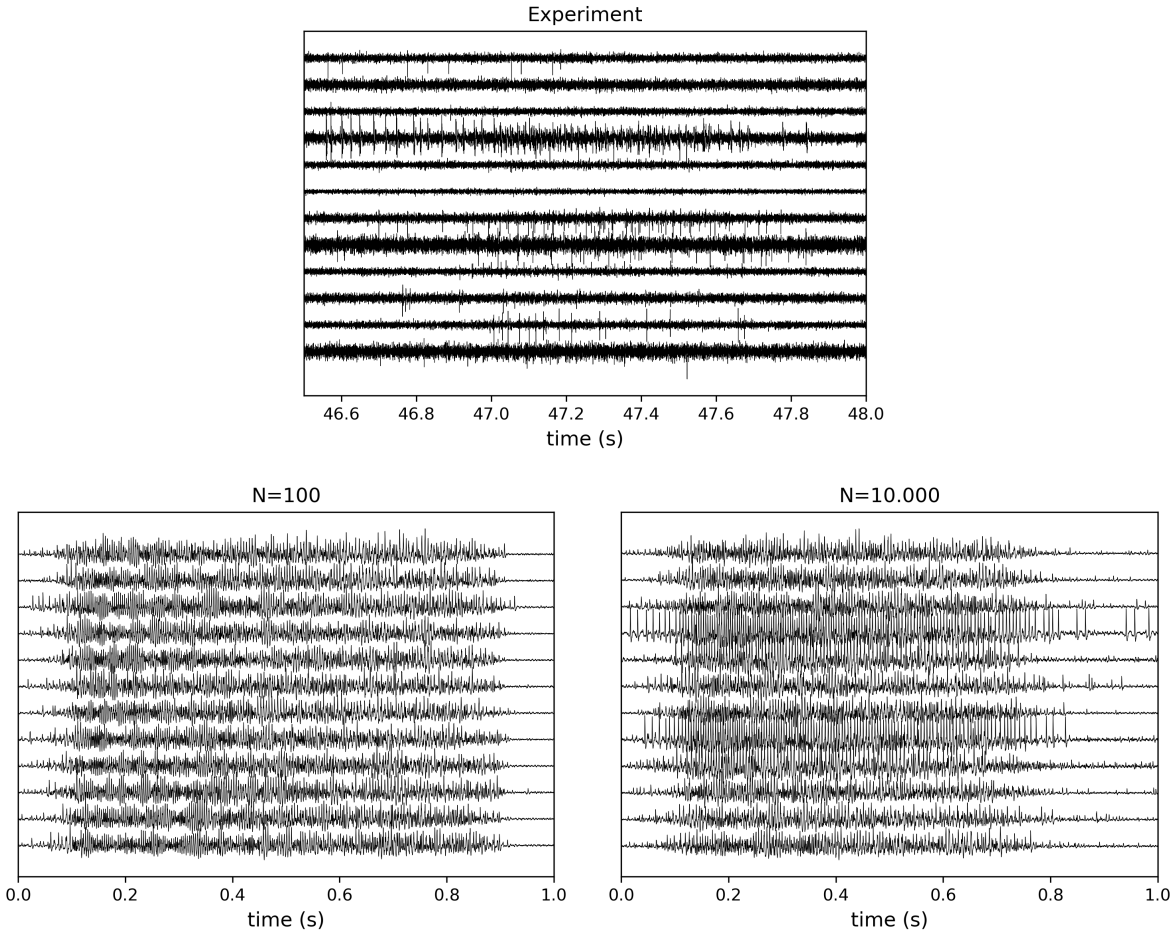

Figure B.6: Voltage recordings within a NB from 12 electrodes of one well from experiments with DS cultures, and simulations with the DS model with 100 neurons and random sparse connectivity, and 10.000 neurons and small-world topology.

B.2.3 DS model with many neurons

We observe large differences between the measurements from different electrodes during an NB in experiments with DS cultures. We cannot simulate these large differences with our model with 100 neurons. We hypothesize that if we increase the number of neurons and use a topology with clusters of highly connected neurons that are less strongly connected to other clusters, like in a small-world network, clusters might become more disconnected from others when we decrease S to simulate DS. We tried this with N=10.000 and P=0.05 in a small-world topology. The result is shown in Figure B.6. We see that there are larger differences between electrodes compared to the simulations with 100 neurons. However, compared to experimental observations, the measurements from the different electrodes are still far too similar in the simulations. This might be because some neuron heterogeneities are not modeled. It might also be because the topology is still not realistic enough. Another approach would be to apply Hebbian learning to the synaptic weights or to include growth dynamics like in the model of Gritsun et al. [17].